博士論文

The physical entity of the synaptic vesicle release site: a Munc13 supramolecular nanoassembly

（シナプス小胞放出部位の物理実体：Munc13 超分子ナノ構造）

坂本　寛和

Summary

The strength of synaptic connections, which is controlled not only postsynaptically but also presynaptically, is a key determinant of neuronal network dynamics. The molecular mechanisms controlling synaptic strength, especially on the presynaptic side, remain elusive. By combining single-synapse glutamate imaging with super-resolution imaging of presynaptic proteins, I find that Munc13-1 molecules form multiple and discrete supramolecular self-assemblies that serve as independent synaptic vesicle release sites by recruiting syntaxin-1 at central glutamatergic synapses. The multiplicity of Munc13-1 supramolecular assemblies affords multiple stable states in presynaptic strength, potentially encoding several bits of information at individual synapses. Therefore, supramolecular assembling confers robustness of synaptic computation in neuronal circuits.

Introduction

Chemical synaptic transmission, which involves neurotransmitter release from presynaptic terminals and neurotransmitter binding to postsynaptic receptors, is fundamental to information processing between neuronal cells [1]. The strength of synaptic connections, which is controlled postsynaptically as well as presynaptically, is heterogeneous among synapses even between same cell pairs [2, 3]. The diversification of synaptic strength among synapses, the synaptic weight, is a key determinant of neuronal network dynamics [4, 5]. The basis of brain functions is a dynamic regulation of the synaptic weight by the synaptic plasticity such as changes in the amount of neurotransmitter release and in the number of postsynaptic receptors [6–10]. The molecular mechanisms controlling synaptic strength, especially on the presynaptic side, remain elusive.

Neurotransmitters are packed into a small vesicle of ~40 nm diameter called synaptic vesicle, and released via exocytosis of the synaptic vesicle at nerve terminals [11]. Neurotransmitter release is well described by quantal theory [1], in which the presynaptic efficacy is determined by two quantal parameters: the number of release sites and the probability of release (Figure 1a). Because of the importance for understanding synaptic computation in neuronal circuits, a long-standing challenge in neuroscience has been to identify the physical basis of these quantal parameters. Each typical presynaptic terminal of central synapses contains hundreds of synaptic vesicles, and only a small population of total vesicles

is readily releasable [12]. The readily releasable vesicles might be attached to a specialized area of the presynaptic terminal known as the active zone (AZ) which contains electron-dense materials precisely opposing to postsynaptic structures [13]. Electrophysiological studies combined with histological examinations originally showed that the number of quantal release sites agrees well with the number of anatomically identified synaptic contacts, each of which contains only one AZ, leading to the conclusion that an AZ structurally corresponds to the quantal release site [14–17] (Figure 1b). However, several studies have suggested that multiple synaptic vesicles are simultaneously released from each presynaptic terminal in conventional central synapses [18–23]; hence, multiple quantal release sites may be organized within each AZ (Figure 1c). The physical basis for these quantal release sites remains controversial [24, 25].

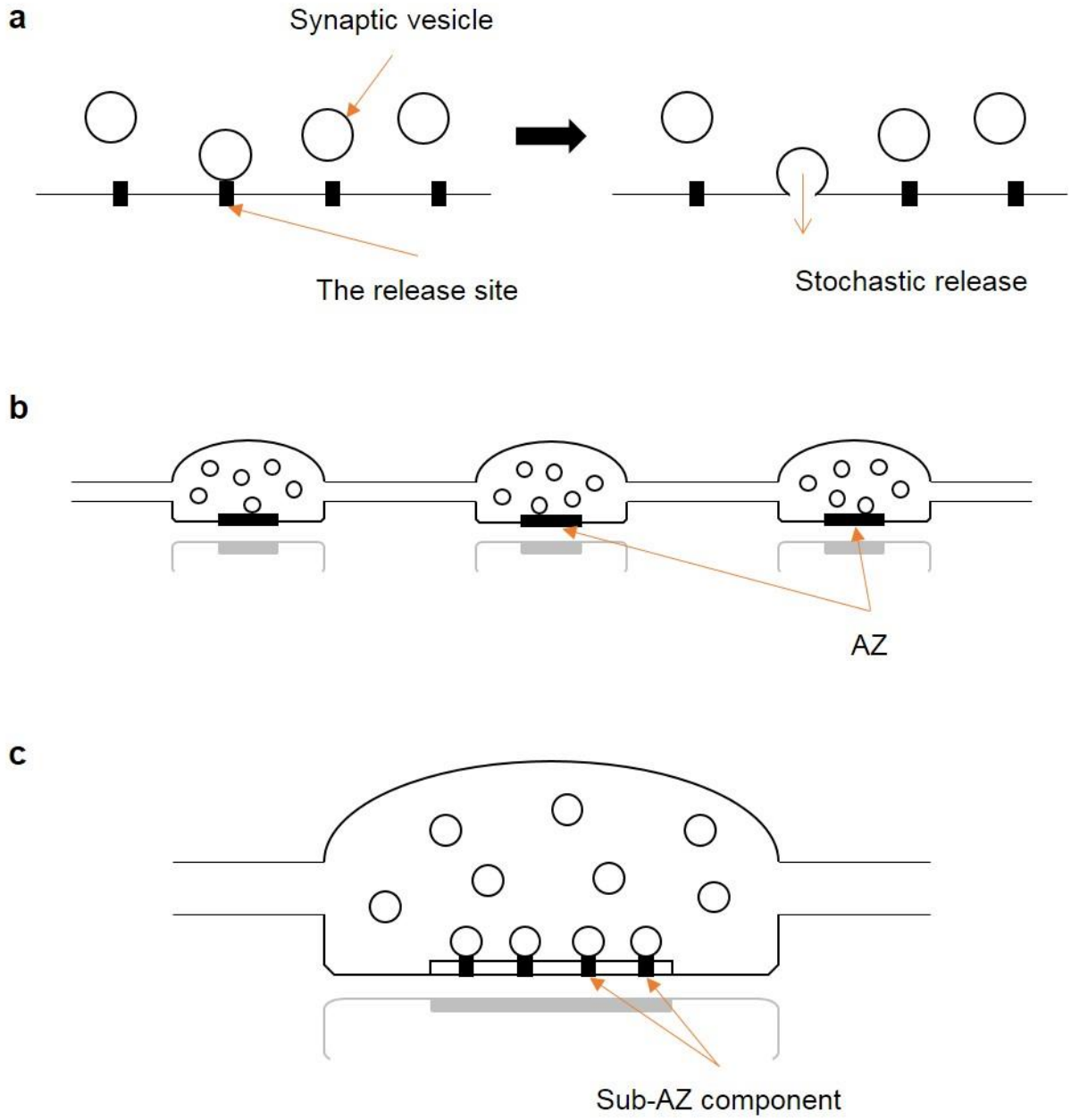

Figure 1 | The synaptic vesicle release site in the quantum hypothesis. (**a**) Schematic diagram for quantal release of neurotransmitter described in quantum hypothesis [1]. The release of neurotransmitter occurs only when synaptic vesicle meets reactive site on the surface of presynaptic plasma membrane, "the release site". The finite number of release sites (*N*) and the probability of release at each site (*P*) determine the synaptic strength. (**b, c**) Schematic diagrams for potential morphological correlates for the release sites. The presynaptic active zone (AZ) (**b**) or sub-AZ component (**c**) may structurally correspond to a binomial unit of neurotransmitter release.

In central synapses, the AZs are sub-micrometer planar structures facing the postsynaptic density across synaptic cleft [13]. They consist of a large number of synaptic proteins [26, 27]. There are several evolutionarily conserved core proteins, including Munc13, RIM, RIMBP, α-Liprin, and CAST/ELKS, and two vertebrate specific proteins, Bassoon and Aczonin/Piccolo in the AZ [28]. Also, the AZs contain membrane proteins essential for regulating synaptic vesicle exocytosis, including syntaxin-1, a soluble N-ethylmaleimide-sensitive-factor attachment receptor (SNARE) protein, and voltage dependent calcium channels. Among these core active zone proteins, Munc13 is particularly essential for synaptic vesicle exocytosis, because synaptic vesicle exocytosis is completely abolished in Munc13 knockout synapses [29–32]. There should be no doubt that Munc13 participates in organization of synaptic vesicle release sites.

Because of the small size of the synapses, an electron microscopy imaging is a common method to analyze the ultrastructure inside the synapses [13]. Electron microscopy with immuno-gold labeling affords nanometer scale localization of AZ proteins [33–35]. However, it is difficult to achieve three-dimensional (3D) localization analysis of AZ proteins with immuno-gold labeling. Furthermore, it is typically difficult to achieve high density immuno-gold labeling on fixed specimens for electron microscopy because of inefficiency in antibody labeling, limiting the absolute quantification of molecular number and distribution. Although immunofluorescence methods with a conventional optical microscopy are widely used to study

localization of synaptic molecules, a conventional optical microscopy imaging is not suitable for analyzing molecular organization at the AZ because it has the limited resolution of ~300 nm due to the diffraction of light. The recent development of super-resolution microscopy enables optical imaging of immunofluorescent specimens with sub-diffraction-limit resolution [36, 37], providing a convenient alternative to electron microscopy imaging with immuno-gold labeling. Among many super-resolution imaging methods, stochastic optical reconstruction microscopy (STORM), a single-molecule localization imaging technique, provides the highest spatial resolution [38–40]. Furthermore, STORM enables multi-color and 3D imaging [41, 42] and has been successfully applied to visualize nanoscale organization of synaptic proteins in synapses [43].

Most previous studies addressing presynaptic mechanisms have relied on an analysis of the ensemble postsynaptic responses of many synapses, not on direct examination of neurotransmitter release at individual synapses. By contrast, I reason that it is important to directly determine the quantal parameters for neurotransmitter release at the single synapse level. Thus, I here develop a novel method to evaluate the quantal parameters of a single synapse using a glutamate imaging technique with an enhanced glutamate optical sensor (eEOS) [44], and find that a multiple number of quantal release sites for individual synapses enable multivesicular release on the arrival of single action potential. To clarify the molecular correlates, I combine this approach with STORM imaging of AZ proteins, and identify a

nanoscale supramolecular assembly of the AZ protein Munc13-1 as a candidate for the physical entity that constitutes the quantal release site (Figure 2).

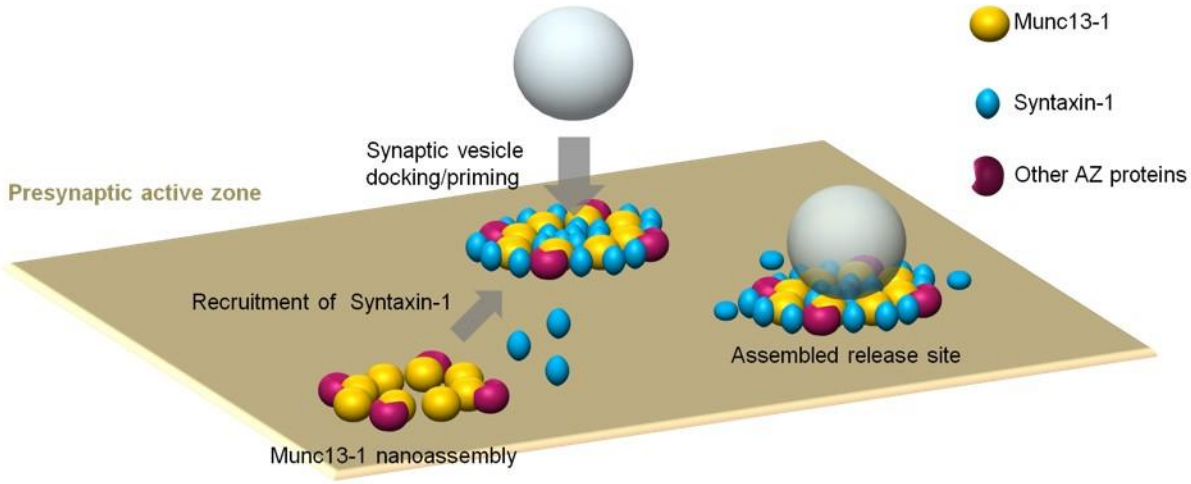

Figure 2 | Hypothetical supramolecular assembling model for the synaptic vesicle release site. An illustration of the supramolecular synaptic vesicle release site model. Munc13-1 molecules are recruited to the active zone (AZ) by binding to RIM or other AZ proteins and then autonomously form a nanosized supramolecular assembly termed "Munc13-1 nanoassembly". The Munc13-1 nanoassembly recruits and opens syntaxin-1. This process may require Munc18-1, although this is not shown in this illustration. The supramolecular assembly effectively and locally provides open syntaxin-1 molecules for forming active SNARE complexes on a synaptic vesicle, and therefore specifies the site for synaptic vesicle docking, priming, and release. Such assemblies are discretely and independently organized within the AZ, and may be arranged in a highly ordered fashion.

Methods

Cell culture.

All protocols used in this study were performed in accordance with the policies of the Animal Ethics Committee of the University of Tokyo (Approval Number: med-P14-058). For primary hippocampal neuronal cultures, neuronal cells were obtained from embryonic day 20–21 Sprague Dawley rats according to a general method [45]. The embryos were decapitated, and the hippocampi were dissected, finely minced, and then treated with trypsin (Thermo Fisher Scientific) and DNase I (Sigma-Aldrich). The dissociated neuronal cells were plated onto glial cell monolayers cultured on a coverslip (Matsunami glass) coated with laminin (Thermo Fisher Scientific) and poly-L-lysine (Nacalai Tesque). Neuronal cultures were maintained in Neurobasal A medium supplemented with B-27 supplement (Thermo Fisher Scientific), 0.5 mM Glutamax (Thermo Fisher Scientific), 1 mM sodium pyruvate (Nacalai Tesque), and 1% penicillin/streptomycin (Nacalai Tesque) at 37°C under 5% CO_2. Cytosine β-D-arabinofuranoside (Sigma-Aldrich) was added to the culture medium, a final concentration of 2.5–5 μM, at 2 days *in vitro*. Glial cells, 293T cells, and COS7 cells were maintained in DMEM (Wako) supplemented with 10% FBS, 4 mM L-glutamine (Wako), 1 mM sodium pyruvate, and 1% penicillin/streptomycin at 37°C under 5% CO_2.

Viral vector construction and infection.

Using the EPRIL method [46], shRNA constructs against Munc13-1 and RIM1 were generated

from 3′-untranslated (UTR) regions of their cDNAs (rat *Unc13a* and *Rims1*, respectively). As a control, an shRNA construct was generated from a coding sequence of the firefly luciferase. The shRNA constructs were subcloned into lentiviral vectors or adeno-associated virus (AAV) vectors with the human U6 promoter. Viral particles were produced by transfection of 293T cells with viral vectors and helper plasmids (Addgene, psPAX2, and pMD2.G for lentiviral vectors; pAAV-RC and pHelper for AAV vectors). Lentiviral particles were harvested 48 h after transfection by collecting the medium and concentrated by centrifugation. The AAV particles were harvested from lysates of transfected cells and purified by ultracentrifugation. Purified viral particles were resuspended in the medium for neuronal cultures and stored at −80°C. Viral particles were added to the neuronal cultures at 11–14 days and kept at least 10 days for imaging experiments. For minimizing of off-target effects, multiple sequences of shRNA constructs were used. The individual sequences of shRNA used were as follows:

shMunc13-1_1: CTTCGAGCTGATCCAGGAGGT

shMunc13-1_2: CTTCCTGATTCTTCCGGGAG

shMunc13-1_3: CTCCAAATCCAGGCAGGAAA

shRIM1_1: GTCCCAATTGTTGTTTAAAA

shRIM1_2: CTCACTCTGTGAAAAGGTGT

shRIM1_3: TTCTTCAGTTCTGTGTGCTTT

shRIM1_4: CAAGCAGTGTTGTTTCCCTA

shRIM1_5: TTCACATGTTTCTGCACAGAC

All shRNA constructs were confirmed using immunocytochemistry to knockdown their target molecules.

Glutamate imaging.

To visualize glutamate dynamics, an enhanced glutamate optical sensor (eEOS) [44]. eEOS consists of a recombinant protein of GluA2 S1S2 domain carrying a cysteine mutation at position 448 glycine residue and Alexa Fluor 488 dye. Purification and biotinylation of eEOS and BoNT/C-H_C were performed as described previously [44, 47]. For making the complex for targeting to the neuronal cell membrane, biotinylated eEOS and biotinylated BoNT/C-H_C were mixed with streptavidin (Vector) at a molar ratio of 2:1:1, respectively. The complex was frozen in liquid nitrogen and stored at −80°C. Cultured neurons were incubated with the complex dissolved in HBS (25 mM HEPES, 125 mM NaCl, 2.5 mM KCl, 2 mM $CaCl_2$, 1 mM $MgCl_2$, 25 mM D-glucose, 10 mM ascorbate, 3 mM myo-inositol, and 2 mM sodium pyruvate, pH 7.4) at a final concentration of 1 μM at room temperature (RT) for 10 min. After incubation, neurons were washed several times with HBS and then used for imaging experiments.

Glutamate imaging experiments were carried out on an Olympus IX-71 inverted microscope. The specimens were illuminated with a blue LED light source passed through a Uniblitz mechanical shutter (Vincent). Fluorescence was imaged with a ×100 oil immersion objective (1.40 NA, Olympus) onto a back-illuminated, 16-bit electron multiplying charge-

coupled device (EMCCD) camera (iXon, Andor). The detector electronics were configured to use 2 × 2 element on-chip binning and frame transfer mode. The acquisition frame rate was set at 20 Hz, unless otherwise stated. In some experiments requiring high time resolution, the acquisition frame rate was set at 50 Hz. The EMCCD camera shutter was opened synchronously with a Uniblitz mechanical shutter. The filter set used was U-MGFPHQ (Olympus).

During glutamate imaging, 100 µM GYKI52466 (Tocris Bioscience), 50 µM D-AP5 (Tocris Bioscience), and 200 nM SYM2081 (Tocris Bioscience) were added to HBS to block ionotropic glutamate receptors to prevent spontaneous firing and recurrent activity. In some experiments, the concentration of divalent cations was varied in a range of 0.5–4 mM for manipulating the release probability. The potassium channel blocker 4-aminopyridine (4-AP, Nacalai Tesque) was also added at a final concentration of 20 µM to acquire a condition of high release probability when necessary. To evoke an action potential, electrical stimulation was delivered via two parallel platinum electrodes 1.4 mm apart for 0.5 ms (5 V⁄mm). The stimulation intensity was set to a value much above the firing threshold (2 V⁄mm) determined by calcium imaging using a low affinity calcium indicator, Fluo4-FF, AM (Thermo Fisher Scientific). Sample drift in z-direction was manually corrected during experiments. All imaging experiments were carried out at RT.

Analysis of glutamate imaging data.

Image analysis was performed using ImageJ software (NIH). All image processing was carried

out on 32-bit floating-point images. Sample drift during recording was corrected using the StackReg plugin for ImageJ. To obtain images of the fluorescence responses ($\Delta F/F_0$, % increase in fluorescence intensities relative to the basal intensities) of eEOS (glutamate signals), each fluorescence image of eEOS was divided by an averaged baseline fluorescence image. The obtained glutamate signal images were then smoothed with a Gaussian spatial filter of 0.32 μm to reduce the image noise. The synaptic sites were identified by post hoc immunocytochemical analysis of bassoon (described below). To ensure single-synapse analysis, only synapses spatially resolved from neighboring synapses were analyzed. Square regions of interest (ROIs) of 0.96 × 0.96 μm (3 × 3 pixels, 2 × 2 camera binning) were positioned at the centre of the synaptic site. Non-synaptic regions in the vicinity of synaptic regions were then positioned to correct the contributions of diffused glutamate signals and photobleaching. When synapses showed a rundown of glutamate release during recording, the recording was discarded. In my experimental conditions, the main source of imaging noise was shot noise; therefore, the background noise variance could be linearly estimated from the eEOS fluorescence intensity of the ROI. The values of estimated noise variance (and SD) were used for determining successful release events and for fluctuation analysis described below.

For spontaneous release analysis, the eEOS fluorescence responses were measured at 50 Hz imaging rate in the presence of 1 μM tetrodotoxin with 200 mM sucrose. Time-series of glutamate signals data were moving averaged over three camera frames. Subsequently, the

glutamate signals above the threshold value lasting for 100 msec (five camera frames) were defined as release events. The threshold value was set relative to SD of the moving-averaged baseline noise. We adopted the threshold value of 2.0.

For detection of the successful release events under the low release probability conditions, the eEOS fluorescence responses were measured at 50 Hz imaging rate, while electrical stimulation was applied at 1 Hz. To attain low release probability conditions, extracellular Ca^{2+} concentration ($[Ca^{2+}]_e$) was reduced to 0.5–1 mM, and $[Mg^{2+}]_e$ was elevated to 2–2.5 mM. The glutamate signals >3.0 times above the SD of the background noise lasting for 60 msec (three camera frames) immediately after electrical stimulation were defined as successful events.

The quantal parameters, the number of functional release sites (*N*), the release probability at each site (*P*), and the quantal amplitude of glutamate signals (*Q*), of single synapses were estimated by applying fluctuation analysis based on the quantal release model [1, 48–53] to single synapse glutamate imaging data. To estimate *Q*, action potential-evoked glutamate signals under low release probability conditions were measured, a total of at least 150 responses, and then the background subtracted variance (σ^2) and the mean glutamate signals (*M*) were calculated. To acquire low release probability conditions, $[Ca^{2+}]_e$ was reduced to 0.5–1 mM, and $[Mg^{2+}]_e$ was elevated to 2–2.5 mM. Under such conditions, the relationship between σ^2 and *M* was approximately linear, with a slope that is equal to the apparent quantal signal amplitude of glutamate release (*Q'*).

$$\sigma^2 = Q'M. \quad (1)$$

Q is then calculated as

$$Q = Q'/(1 + {CV_Q}^2), \quad (2)$$

where CV_Q (= 0.28) is the coefficient of variation of the quantal amplitude and Q is the quantal amplitude to be determined. The CV_Q value was determined from spontaneous miniature events of glutamate release in five synapses. In glutamate imaging analysis at single synapses, CV_Q was assumed to arise only from *intrasite* variability [53], since all the release sites are formed in the same AZ.

Multiple-probability fluctuation analysis [51–53] was applied to estimate three presynaptic parameters (*N*, *P*, and *Q*). To acquire multiple release probability conditions, glutamate signals evoked at 0.05–0.5 Hz were recorded in different Ca^{2+}- and Mg^{2+}-containing solutions. In a typical experiment, it was important that 4-AP was added to the extracellular solution for acquiring a high *P* condition, which is essential for a parabolic fit giving an accurate estimation of *N*. At each release probability condition, 40–100 responses were recorded, and then σ^2 and *M* were calculated. The relationship between them was fit with a binomial model of release:

$$\sigma^2 = Q'M - \frac{1}{N}M^2, \quad (3)$$

where Q' is the apparent quantal signal amplitude of glutamate release (see Eq. 2). The *P* at each $[Ca^{2+}]_e$ condition was obtained by dividing M by NQ. Parabolic fits were accepted when

the maximum release probability was >0.45 to ensure an accurate estimation of N (53 of 71 synapses satisfied this criterion). The P was assumed to be uniform across release sites. The error estimates of σ^2 were calculated using *h*-statistics as previously described [53]. The standard errors of estimates of Q and N were estimated by bootstrap resampling analysis of 10,000 replications for each data set.

The success rate of release (at least one vesicle released) at the synapse (P_s) was measured and compared with the predicted success rate inferred from the estimated quantal parameters. The theoretical success rate of glutamate release was calculated as follows:

$$P_s = 1 - (1 - P)^N. \quad (4)$$

For analysis of glutamate signals in response to high-frequency repetitive stimuli, the time course of the fluorescence responses of eEOS,$S(t)$, was subjected to deconvolution analysis [54, 55]. The decay time constant of eEOS fluorescence responses was estimated from a single action potential-evoked response to be τ = 170 msec. To simplify the procedure, we assumed that the glutamate signals occurred instantaneously. Therefore, $S(t)$ can be expressed as a convolution of the signals in response to glutamate release, $r(t)$, and the exponential decay function with a time constant τ, as follows:

$$S(t) = \int_0^t r(t') \cdot e^{-\frac{t-t'}{\tau}} dt'. \quad (5)$$

Then, $S(t)$ can be deconvolved using the following formula:

$$r(t) = \frac{dS(t)}{dt} + \frac{S(t)}{\tau}. \quad (6)$$

The estimated deconvolved signal $r(t)$ should be a linear measure of glutamate release if eEOS is far from saturation. Since the recorded synaptic glutamate signal amplitudes were below 50%, a value far below the maximal eEOS fluorescence responses (>1,000%), the glutamate-bound fraction of eEOS was hence ignored. By dividing $r(t)$ by Q estimated with fluctuation analysis, the vesicular release rate $v(t)$ can be calculated as follows:

$$v(t) = \left(\frac{dS(t)}{dt} + \frac{S(t)}{\tau}\right)/Q. \quad (7)$$

For estimation of the number of readily releasable vesicles (N_{RRV}), synaptic glutamate release was elicited with a brief burst of high-frequency stimulation consisting of 20 pulses at 50 Hz. The burst stimulation was repeated five times per synapse. Because the sufficient depletion is important for accurate estimation, $[Ca^{2+}]_e$ was raised to 4 mM, and 4-AP was added to the extracellular solution. The vesicular release rate was calculated by deconvolution (Eq. 7) from eEOS fluorescence responses, and then integrated to provide the time course of cumulative vesicular release. Subsequently, the sizes of the fast and slow components of released vesicles during high-frequency stimuli were estimated from the cumulative release by using back-extrapolation of cumulative release from a steady state to time 0. The size of the fast component corresponds to N_{RRV}; the slow steady-state components of cumulative release represents the reloading of releasable vesicles to an empty release site, or "ongoing priming" during stimulation [56]. To confirm the efficiency of the depletion protocol, I applied the correction method for incomplete pool depletion as described previously [57]. The estimated fraction

required for correction was nearly zero (2.7 ± 3.7% of the total estimated pool size, n = 71 synapses), indicating a near complete depletion. Therefore, the values without correction were used. The standard error for the estimate of N_{RRV} was calculated for each synapse from combined variance arisen from trial-to-trial variation ($\sigma_{trial}{}^2$) and variation in Q estimates as

$$\sqrt{\frac{\sigma_{trial}{}^2}{n} + \left(\frac{SEM_Q}{Q}\right)^2 N_{RRV}{}^2}, \qquad (8)$$

where n is the number of trials, and SEM_Q is standard error of Q, which was estimated by fluctuation analysis with bootstrap resampling.

Antibodies.

Mouse monoclonal Munc13-1 antibodies (clones: 11B-10G and 5D-7G) were raised against residues 1-320 of Munc13-1 expressed as a His-tagged recombinant protein. Mouse monoclonal Munc13-1 antibodies (clone: 2A-5) was raised against MUN domain of Munc13-1. The following commercially available primary antibodies were used: anti-bassoon (clone: SAP7F407, Enzo Life Sciences), anti-syntaxin-1 (clone: 78.2, Synaptic Systems), anti-syntaxin-1A (clone: 78.3, Synaptic Systems), anti-VGLUT1 (135 302, Synaptic Systems), anti-RIM1 (140 013, Synaptic Systems), anti-piccolo (142 003, Synaptic Systems) and anti-ERC1b/2 (143 003, Synaptic Systems).

All secondary antibodies used in this study were labeled with N-hydroxysuccinimide (NHS)-activated fluorescent dyes, Alexa Fluor (Alexa-) 405, 488, 555, 647 or DyLight 755

(Thermo Fisher Scientific). For mouse monoclonal antibodies, highly cross-adsorbed subtype-specific secondary antibodies (Jackson ImmunoResearch) were used. For rabbit polyclonal antibodies, highly cross-adsorbed $F(ab')_2$ fragments (Jackson ImmunoResearch) were used.

Immunocytochemistry.

For most of the immunostaining experiments, cells were fixed with PBS containing 1–4% paraformaldehyde (PFA; Wako) for 15 min, and then permeabilized with pre-cooled (4°C) PBS containing 0.25% Triton-X. For immunostaining of synaptic syntaxin-1, cells were fixed with pre-cooled (−20°C) methanol/acetone solution for 5 min or fixed with 1% PFA for 15 min on ice and permeabilized with 0.1% saponin (Sigma). After blocking with PBS containing 0.3% BSA, primary antibodies were incubated in PBS containing 0.3% BSA for 1 h. After being washed, the cells were incubated with fluorescent dye-labeled secondary antibodies in PBS containing 0.3% BSA for 30 min. Finally, after extensive washing, specimens were post-fixed with 4% PFA. All these procedures were carried out at RT. Until used in imaging experiments, specimens were stored at 4°C in PBS containing 0.1% NaN_3.

Standard immunofluorescence imaging experiments were carried out using an Olympus IX-71 inverted microscope with a ×100 oil immersion objective and a xenon arc lamp. Images were acquired with a back-illuminated EMCCD camera (iXon, Andor). The filter set for Alexa-488 was U-MGFPHQ, for Alexa-555 it was U-MRFPHQ (Olympus), and for Alexa-647 it was Cy5-4040C (Semrock).

To analyze the immunofluorescence of synaptic proteins, the specimens were routinely co-labeled with a monoclonal antibody (clone: SAP7F407) for the presynaptic AZ marker bassoon because it showed a low non-specific labeling and a large tolerance for fixation protocols, making it a good standard synaptic marker. To ensure single-synapse analysis, only synapses spatially resolved from neighboring synapses were analyzed. To evaluate the immunofluorescence intensity of synaptic proteins at synapses, the fluorescence at non-synaptic regions in the vicinity of synaptic sites was considered non-specific labeling, and that value was subtracted. This assumption was confirmed in knockdown experiments that showed similar non-specific labeling at non-synaptic regions in knockdown neurons.

Estimation of the number of Munc13-1 molecules at synapses.

First, the fluorescence intensity of single Alexa-647 molecules (FI_{647}) was evaluated by single-molecule imaging. A collagen- and poly-L-lysine-coated coverslip was incubated with 1% $NaBH_4$ for 30 min, then with 1 nM Alexa-647 NHS ester for 10 min, and washed twice with sterile water. Subsequently, the samples were immersed in high sugar HEPES buffer (50 mM HEPES, 10 mM NaCl, 60% sucrose, 10% glucose, pH 8.0). Imaging experiments were performed using a custom-built microscope with a ×100 oil immersion objective (1.40 NA, Olympus), an EMCCD camera (iXon3 860, Andor), and a piezo controller (P-733.3 XYZ Piezo Nanopositioning Stage, PI). Alexa-647 molecules were excited using a 640 nm laser beam (OBIS, Coherent Inc.) passed through a Cy5 excitation filter (Semrock). With these procedures,

spatially distinct fluorescent spots were observed on the coverslip. Almost all fluorescent spots bleached in one step, supporting the assumption that the observed fluorescent spots were single Alexa-647 molecules. FI_{647} was then determined, by subtracting the background intensity, to be 280 ± 78 (arbitrary unit, a.u.) (mean ± SD, n = 55).

Next, a Munc13-1 monoclonal antibody (clone: 11B-10G) was labeled with the Alexa-647 NHS ester. The labeling efficiency was approximately 300% when measured with a spectrofluorometer. The Alexa-647-labeled antibodies were non-specifically adsorbed on a coverslip treated with 1% $NaBH_4$. As with Alexa-647 single-molecule imaging, spatially distinct fluorescent spots were observed in these preparations. However, most of these fluorescent spots did not bleach in one step as expected. The fluorescence intensity of a single Alexa-647-labeled monoclonal antibody against Munc13-1 (FI_{ab}) was then determined, after subtracting the background intensity, to be 782 ± 578 (a.u.) (mean ± SD, n = 57), 279% of FI_{647}. This value for the labeling efficiency was consistent with the estimation determined using a spectrofluorometer.

Finally, the immunofluorescence intensity of Munc13-1 at synapses (FI_{syn}) was evaluated by direct immunostaining of neurons using the Alexa-647-labeled antibody to Munc13-1. FI_{syn} was determined, after subtracting the fluorescence intensity of neighboring non-synaptic regions, to be 35,000 ± 22,300 (a.u., mean ± SD, n = 123). For evaluating the effect of refractive index mismatch on the estimation of fluorescent intensity at the synapses, neuronal surfaces

were directly labeled with Alexa-647 NHS ester. The FI_{647} was reduced to 83% on neurons compared with that on the surface of glass. Therefore, the number of Munc13-1 molecules within synapses (n_{syn}) can be estimated from the equation below:

$$n_{syn} = FI_{syn} / (FI_{ab} \times 0.83)$$

$$= 35{,}000/ (782 \times 0.83)$$

$$\approx 54$$

This estimation might be a lower limit for the number of Munc13-1 molecules per synapses considering that some epitopes might be unavailable.

STORM imaging.

For STORM imaging without activator dyes [39, 40], specimens were double immunostained with two primary antibodies and two secondary antibodies labeled with Alexa-647 or DyLight 755. For STORM imaging with activator dyes [41], specimens were immunostained with secondary antibodies bearing Alexa-647/405 or Alexa-647/488. The dye labeling efficiency of the secondary antibodies was optimized to the primary antibodies of interest. To analyze the nanoscale molecular architecture with super-resolution microscopy, it is important to label most molecules (epitopes) of interest as much as possible to avoid misinterpretations due to undersampling. To this end, first, optimal concentrations of fixative were determined to avoid epitope masking during fixation. Strong fixation sometimes led to dim or negative labeling of AZ proteins, presumably due to the masking of epitopes because of high protein concentrations

in the AZ. Next, the concentrations of primary antibodies were titrated to determine the practical concentrations at which available epitopes were saturated with primary antibodies.

Dark-red fluorescent 200 nm beads (F-8810, Thermo Fisher Scientific) were bound to the specimens and used as fiducial marker. The STORM imaging buffer contained 50 mM HEPES (pH 8.0), 10 mM NaCl, 60% sucrose, 10% glucose, 0.1–1% β-mercaptoethanol, 0.5 mg/mL glucose oxidase, and 0.04 mg/mL catalase. High concentrations of sugar (70%) increased the refractive index of the buffer to approximately 1.47. Specimens mounted in STORM imaging buffer were then sandwiched with another small coverslip and sealed with nail polish.

STORM imaging experiments were performed on a custom-built microscope with a ×100 oil immersion objective (1.40 NA, Olympus), an EMCCD camera (iXon3 860, Andor), custom illumination optics, a piezo-positioning stage (P-733.3 XYZ Piezo Nanopositioning Stage, PI), and a custom-made objective holder that minimized mechanical sample drift during experiments. Images, formed by a collecting lens (AC254-250-A-ML, Thorlabs), were relayed onto the camera with a pair of lenses (AC254-100-A-ML, Thorlabs), achieving a pixel size of 192 nm. For 3D astigmatism-based calibration, a cylindrical lens (LJ1558RM-A, f = 300 mm, Thorlabs) was inserted into the detection path after the last lens at an approximate distance of 30 mm from the camera, providing astigmatism with the 0.59 μm difference in vertical and horizontal focal lengths for the object planes. A 640-nm laser beam (OBIS, Coherent Inc.) passed through a Cy5 excitation filter (Semrock) was used to excite Alexa-647 molecules at an

excitation intensity of approximately 5 kW/cm^2. Fluorescence detection of Alexa-647 was achieved using a penta-band dichroic mirror (Semrock) and a bandpass emission filter (710QM80, Omega). A 745-nm pulse laser beam generated with a Chameleon laser (Coherent Inc.) passed through a Cy7 excitation filter (Semrock) was used to excite DyLight 755 molecules at an excitation intensity of approximately 1 kW/cm^2. Fluorescence detection of DyLight 755 was achieved using a penta-band dichroic mirror and a Cy7 emission filter (Semrock).

For STORM imaging without activator dyes, a 405-nm laser beam (OBIS, Coherent Inc.) was used to re-activate Alexa-647 and DyLight 755 molecules from the dark state to the emitting state. The excitation intensity of the 405-nm laser was set to a range of 0.1 to 32 W/cm^2, so that fluorescent signals from activated molecules were not spatially overlapped. A 543-nm laser beam (CNI) was used to activate fluorescent fiducial beads during DyLight 755 imaging, if needed. A series of 50,000–100,000 imaging frames (10–16 ms per frame) for Alexa-647 or 30,000–60,000 imaging frames (25–50 ms per frame) for DyLight 755 were measured for the respective image reconstructions.

For STORM imaging with activator dyes, 405-nm and 488-nm laser beams (OBIS, Coherent Inc.) were used to activate Alexa-647 molecules via Alexa-405 and Alexa-488, respectively. A series of 5,000 imaging frames (10–16 ms per frame) were alternately measured for 488 and 405 channels for a total of 60,000–120,000 imaging frames for image

reconstructions. The excitation intensities of the 488-nm and 405-nm lasers were gradually increased from 0.25 to 8 W/cm^2 and from 1 to 32 W/cm^2, respectively. To minimize crosstalk between the channels used to detect the two colors, the 488 channel was measured first. The crosstalk fractions for different color channels were quantitatively determined using specimens singly labeled with only one of the secondary antibodies.

STORM image reconstruction and analysis.

Localizations of fluorophores were determined using custom-designed software in ImageJ. A 2D Gaussian model was used with the least-square fitting method. The z-axis localizations were determined using 3D astigmatism-based calibration [42]. Sample drift during recording was corrected using fluorescent fiducial markers. Chromatic aberration between Alexa-647 imaging and DyLight 755 imaging was corrected with a chromatic shift vector map that was constructed using fluorescent beads [58]. STORM images were then reconstructed by pixelating single-molecule localization datasets with a 10 nm binning and processed using a 3D Gaussian spatial filter with a radius of 10 nm.

To determine the practical localization precision of 3D-STORM imaging in my settings, I analyzed the single-molecule fluorescence images for Alexa-647 labeled antibodies which were non-specifically bound on the fixed neuronal cell cultures. The number of photons from a single Alexa-647 molecule detected per frame (camera exposure time of 16 ms) was ~3,600 on average; the background counts were 121 photons (per pixel per frame) on average. The

estimated localization precision (in standard deviations) obtained were 9.0 nm in x-axis, 9.7 nm in y-axis, and 19.0 nm in z-axis.

The reproducibility of nanoscale structures in STORM images was verified with a separate dataset, typically using a reconstruction from the first half of the imaging frames and a reconstruction from the last half of the imaging frames. This verification helped to avoid misinterpretation of reconstructed images attributed to incomplete data acquisition for STORM image reconstruction. In most cases using my imaging procedures, Alexa-647 imaging provided robust reproducibility in the reconstruction of nanoscale structures, whereas DyLight 755 imaging provided lower reproducibility, possibly due to a limited number of switching cycles for the DyLight 755 molecules [59]. For this reason, detailed nanoscale molecular structures, such as Munc13-1 nanoassemblies, were evaluated only in Alexa-647 STORM imaging datasets.

For analysis of the spatial distribution of molecules within the AZ, STORM images were rotated in 3D such that the AZ surface faced the front. By using human eyes, the 3D-STORM images were manually rotated in all three axes (y, z, and then x axis) one-by-one on the image display monitor. Initially, data were rotated around the y-axis to find the side view of the AZ (at the point where the apparent short AZ axis is narrowest), then rotated around the z-axis so that the apparent long AZ axis was aligned horizontally, and finally rotated 90 degrees around the x-axis. The validity was evaluated by comparing the manually obtained AZ planes with the

plane numerically estimated by principal component analysis of localization data, showing little differences in inclinations (θ = 4.9 ± 3.0 degrees, n = 18 AZs). The overall resolution on the 2D-projected AZ plane should be affected both by lateral and axial localization precision depending on the degree of inclination of AZ. Therefore, I calculated the overall resolution on the 2D-projected AZ plane as a function of AZ inclination relative to imaging x–y plane (θ):

$$\widehat{\sigma_r} = \sqrt{{\sigma_{xy}}^2 + \frac{1}{2}({\sigma_z}^2 - {\sigma_{xy}}^2)sin^2\theta}. \quad (9)$$

The inclination of AZ plane, which ranged from 10.2 to 86.7 degrees, provides the estimation of σ_r of 9.6–15.0 nm. These correspond to the resolution of 22.6–35.2 nm, suggesting that the resolution of my experiments was enough to analyze the distributions of Munc13-1 nanoassemblies that were separated by ~85 nm from each other. Consistent with this view, the estimate of the inter-assembly distance of Munc13-1 nanoassemblies (84.7 ± 22.7 nm) was little changed (84.1 ± 23.5 nm) when the analysis was limited to AZs with smaller inclination (< 30 degrees, giving the precision of 11.0 nm).

Molecular clustering was confirmed by agglomerative hierarchical method (Ward's method), and then the cluster distribution was evaluated. This analysis was performed using Hierarchical Clustering Package in Mathematica. Pair-correlation function analysis [60] was then applied to STORM imaging data [61, 62] to quantify the spatial auto-correlation of the imaged molecules or the relative distribution of two imaged molecules. The effect of crosstalk

between two color channels in pair-correlation function analysis was corrected using the product density and then calculating $g(r)$ based on stationary point processes [60]. These analyses were performed using custom-designed software in Matlab and Mathematica.

Reconstitution experiments in non-neuronal cells.

The Munc13-1-EGFP expression vector (pEGFP-Munc13-1) was a gift from Dr. Nils Brose (Max Planck Institute). The Munc13-1 expression vector was generated from pEGFP-Munc13-1 by inverse PCR. The coding sequence of TagRFP (Evrogen), the zinc-finger (ZF) domain of rat RIM1α (residues 56-228), and the CAAX motif of KRas (KMSKDGKKKKKKSKTKCVIM) were fused and subcloned into the pcDNA3.1 vector (Thermo Fisher Scientific) (pcDNA-TagRFP-ZF-CAAX). A DNA fragment encoding full-length rat syntaxin-1A was subcloned into the pcDNA3.1 vector (pcDNA-syntaxin-1A). The syntaxin-1A-pHluorin expression vector (pcDNA-Syntaxin-1A-pHluorin) was generated by fusing syntaxin-1A with pHluorin, a pH sensitive mutant of GFP. The expression vector for full-length Munc18-1 was MGC clone #30503.

The 293T and COS7 cells were transfected with the expression vectors mentioned above using X-tremeGENE HP (Roche). One day after transfection, the cells were harvested and plated onto coverslips coated with collagen and poly-L-lysine. One day after plating, the cells were used for live-cell imaging or immunocytochemistry.

Results

Imaging of glutamate release at synapses

To visualize glutamate release at synapses, I used eEOS, a fluorescent glutamate indicator that has a wide dynamic range over 1,000% with a K_d of 50 μM [44]. eEOS was attached to the cell surface of cultured hippocampal neurons using a non-toxic domain of botulinum neurotoxin type C, which specifically binds neuronal ganglioside (Figure 3). Bath applications of glutamate induced spatially homogeneous increases in eEOS fluorescence along the neurons in a dose-dependent manner (Figure 4).

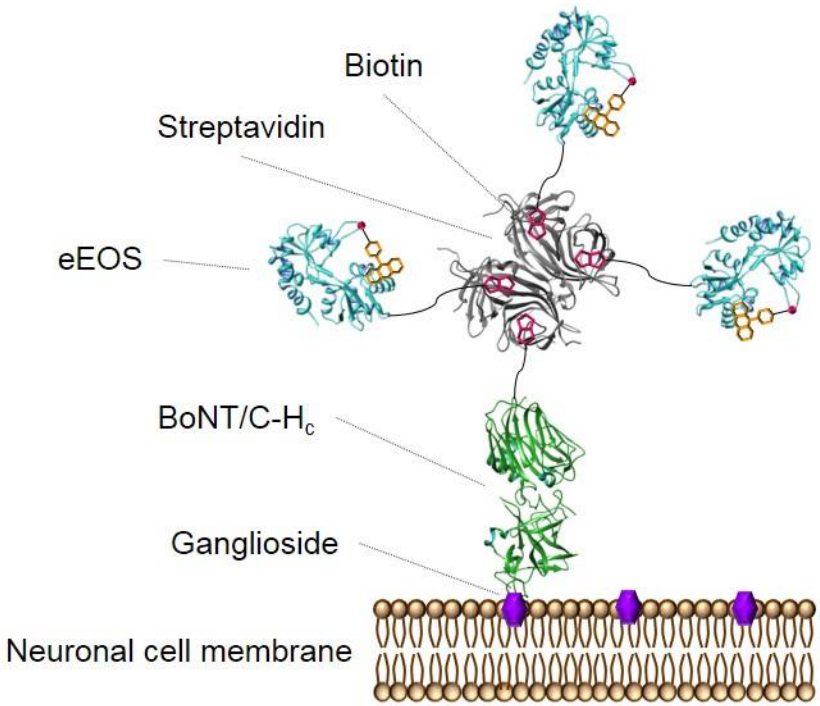

Figure 3 | A strategy targeting eEOS to the neuronal cell surface. A schematic illustration for eEOS (cyan) targeting to the neuronal cell surface using non-toxic heavy chain of botulinum neurotoxin type C (BoNT/C-H_C, green) via biotin-streptavidin interaction. Biotinylated eEOS and biotinylated BoNT/C-H_C were mixed with streptavidin for making complex targeting to the neuronal cell membrane.

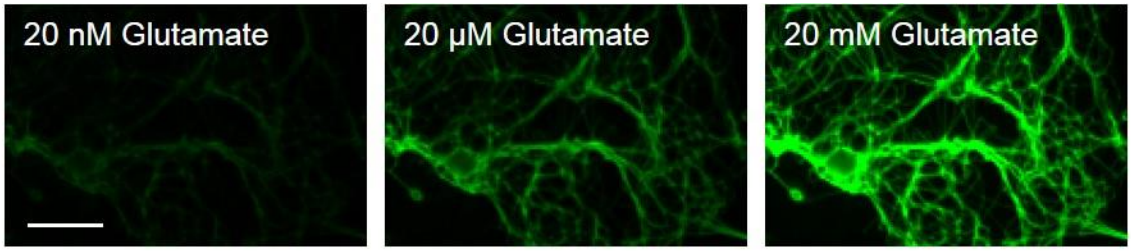

Figure 4 | Properties of eEOS bound on the neuronal cell surface. Fluorescence images of eEOS bound on the neuronal cell surface in the presence of 20 nM (top), 20 µM (middle) and 20 mM (bottom) glutamate, respectively. Bath applications of glutamate induced spatially homogeneous increases in eEOS fluorescence intensity. TBOA, a glutamate transporter inhibitor was applied in bath solution at the concentration of 100 µM . Scale bar, 100 µm.

Concomitant with an action potential elicited by electrical field stimulation, I observed focal, transient eEOS fluorescence responses (i.e., glutamate signals). To examine the location of these glutamate signals, action potential-evoked eEOS responses were averaged over multiple stimuli. The spatial distribution of the averaged glutamate signals corresponded well to that of the immunofluorescence of presynaptic markers, VGLUT1 and bassoon (Figure 5). These results indicate that each discrete glutamate signals represents the release of glutamate from individual presynaptic terminals.

I then inspected synaptic glutamate release in response to single action potentials. I found large trial-to-trial variation characterized by frequent failures of glutamate release (Figure 6). These failures were not due to action potential failures, because suprathreshold electrical stimulation was used. Rather, they reflected the stochastic nature of quantal vesicular release [48].

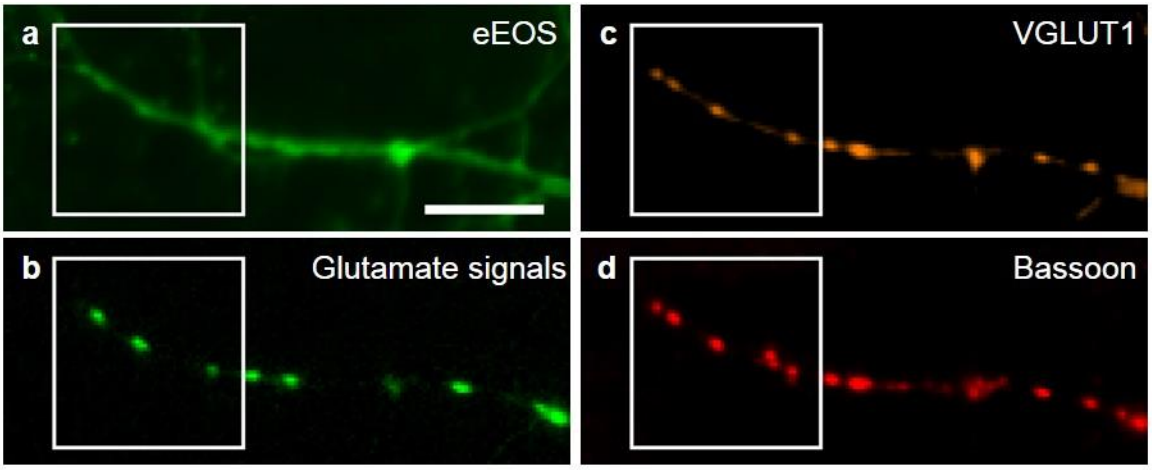

Figure 5 | Imaging of glutamate release at single synapses. (**a**) eEOS attached on the neuronal cell surface. Scale bar, 10 μm. (**b**) Averaged fluorescence responses of eEOS in response to a single stimulus at 2 mM $[Ca^{2+}]_e$. (**c, d**) Immunofluorescence of VGLUT1 (**c**) and bassoon (**d**) in the same region shown in **a**.

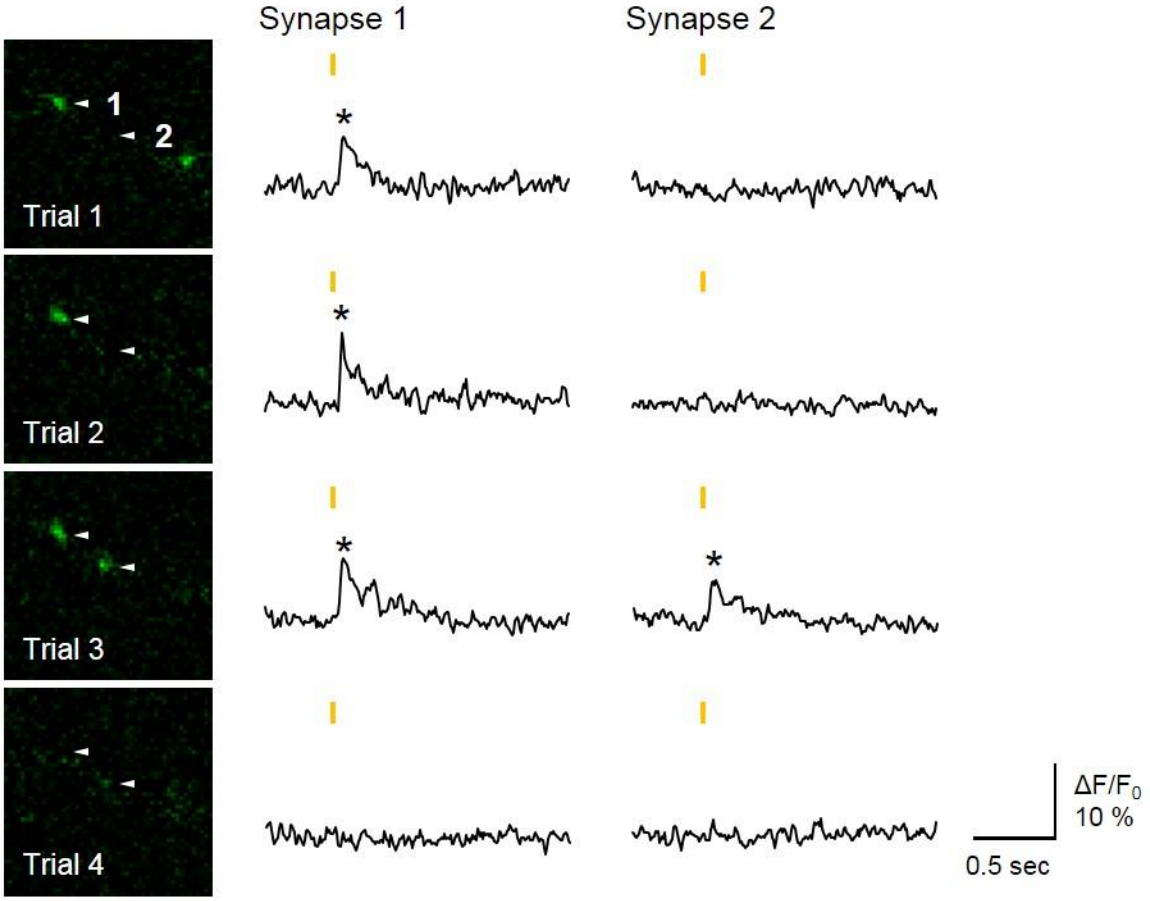

Figure 6 | Trial-to-trial variation in glutamate release at single synapses. Images (left) and time courses (right) of glutamate signals following each single stimulus. Images shown are from the white-boxed regions in Figure 5. Each time course corresponds to each synapse indicated with an arrowhead. Orange vertical bars represent the stimulation timing. Asterisks show successful glutamate release events.

When the extracellular Ca^{2+} concentration ($[Ca^{2+}]_e$) was lowered from 2 mM to 0.5 mM, failure events became dominant, while successful events were still clearly discernible (Figure 7a). Spontaneous “miniature” events of glutamate release were also detected in the presence of tetrodotoxin to block action potentials (Figure 7b). The glutamate signal amplitude of the successful events at 0.5 mM $[Ca^{2+}]_e$ was equivalent to that of the spontaneous “miniature” events at the same synapse (Figure 8). Furthermore, the quantal amplitude of glutamate signals estimated by the fluctuation analysis well accounted for the mean amplitude of the successful events at the same synapses (Figure 8). These results show that the glutamate imaging method can detect quantal glutamate release derived from a single synaptic vesicle.

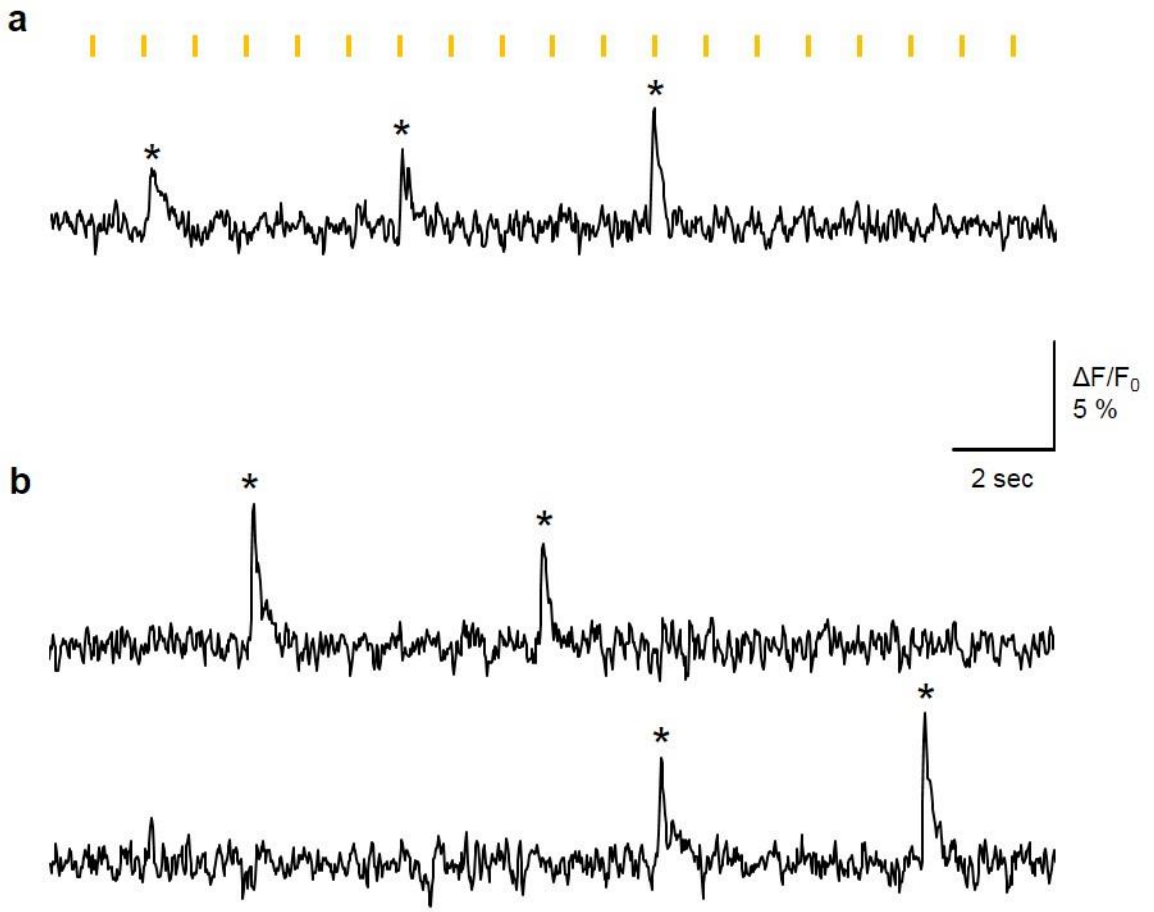

Figure 7 | Detection of quantal glutamate release at single synapses. (**a**) Time course of fluorescence responses of eEOS at a single synapse following 1 Hz stimuli at 0.5 mM $[Ca^{2+}]_e$. Orange bars represent the timing of stimuli. Asterisks show successful glutamate release events. (**b**) Time courses of fluorescence responses of eEOS at a single synapse in the presence of 1 μM tetrodotoxin with 200 mM sucrose. Asterisks show detected spontaneous glutamate release events. Data are obtained from the same synapse in **a** and **b**.

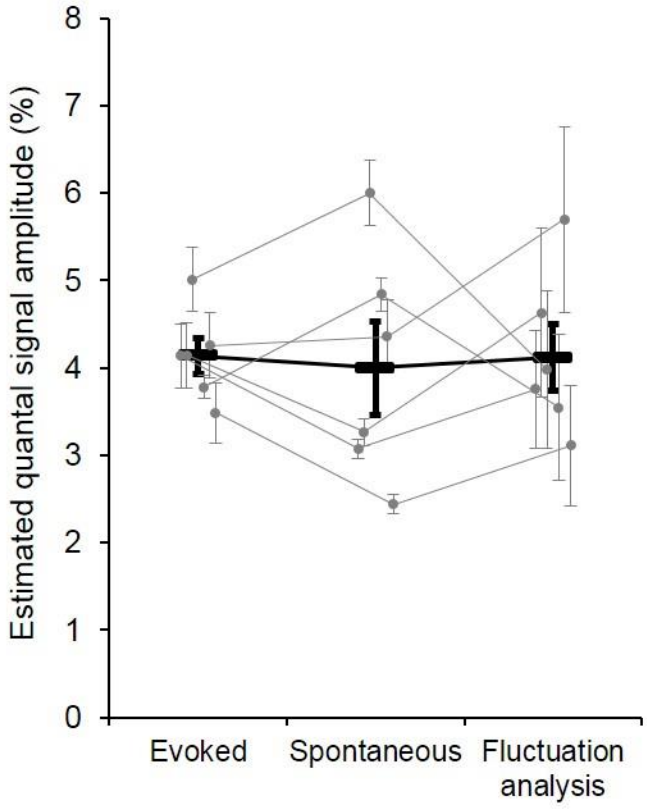

Figure 8 | Comparison of quantal glutamate signal amplitude estimated by three different methods. Quantal amplitude of glutamate signals evaluated by three different methods: analysis of evoked events at low $[Ca^{2+}]_e$, analysis of spontaneous "miniature" events, and fluctuation analysis. Gray symbols indicate the results from individual synapses, and black indicate the mean value of results from all synapses. Data are represented as mean ± SEM. To evaluate standard errors for fluctuation analysis for individual synapse data, bootstrap resampling analysis of 10,000 replications was performed. There is no significant difference between these estimates (Friedman rank sum test, $P = 0.85$, df = 2, $\chi 2 = 0.33$; $n = 6$ synapses from three culture preparations).

Multiple quantal release sites at a synapse

Only a small population of the total vesicles within a presynaptic terminal is readily releasable within a short period of time; this population is often referred to as the readily releasable pool [63]. I estimated the number of readily releasable vesicles (N_{RRV}) by applying a brief burst of electrical stimulation. To ensure a high rate of glutamate vesicular release, I used a stimulation frequency of 50 Hz with $[Ca^{2+}]_e$ increased to 4 mM in the presence of 4-aminopyridine (4-AP). Glutamate signals reached a peak within 0.1 s after the initiation of stimulation, and then slowly decayed (Figure 9a). To obtain the time course of the cumulative vesicular release, I

deconvolved the glutamate signals using the decay kinetics of eEOS and then performed a calibration using the quantal amplitude (Figure 9b). The cumulative release showed an immediate rapid release (fast component) that was followed by a slow steady release (slow component) (Figure 9c). The fast component corresponds to the release of the readily releasable vesicles, and the slow component represents the release of newly replenished vesicles during the stimuli [56]. The N_{RRV} varied from synapse to synapse with an average of 5.5 ± 3.2 (n = 71 synapses).

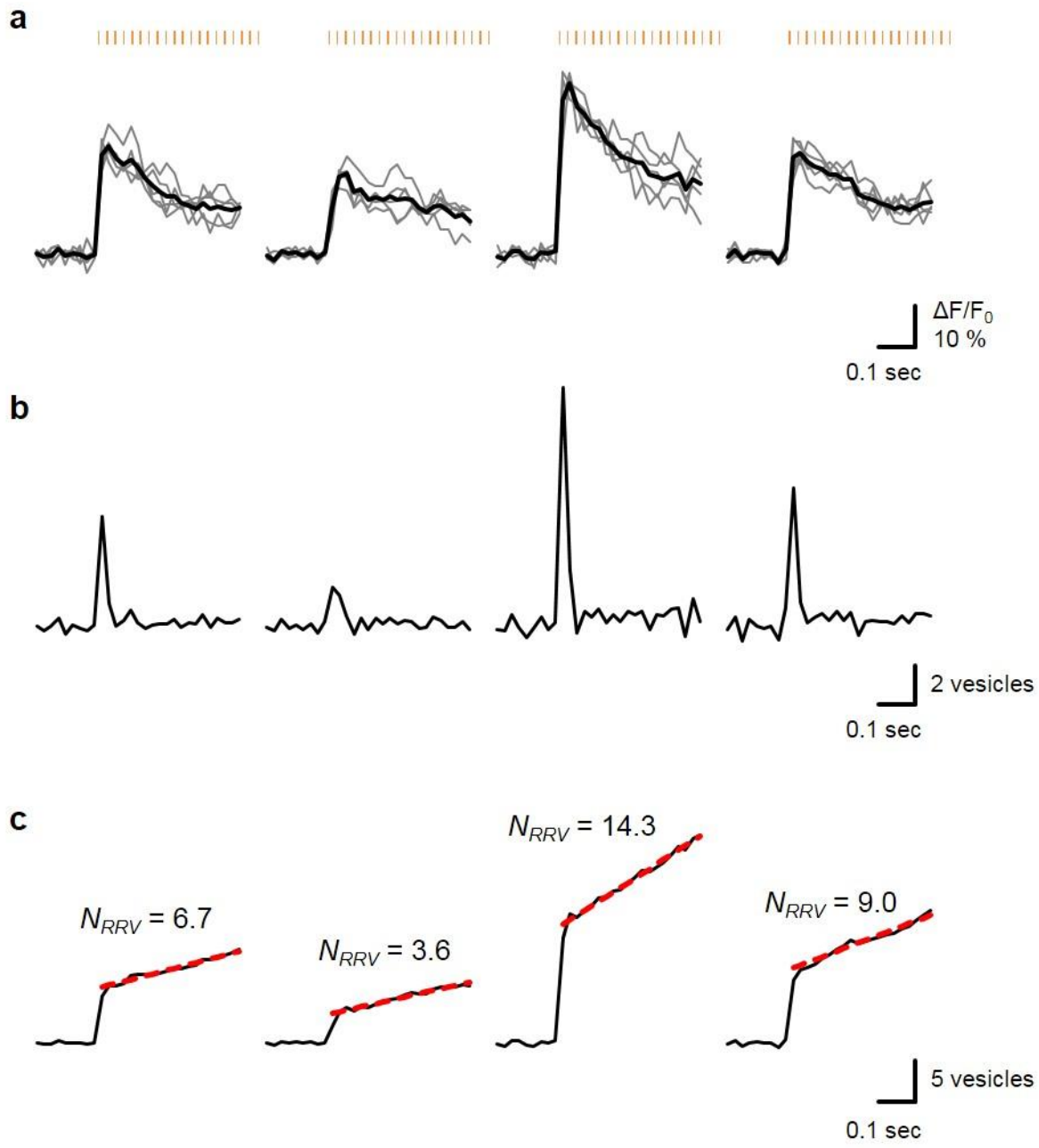

Figure 9 | Counting the number of releasable vesicles at single synapses by deconvolution analysis of glutamate imaging. (**a**) Time courses of fluorescence responses of eEOS at four single synapses evoked by 20 stimuli at 50 Hz with 4 mM $[Ca^{2+}]_e$ in the presence of 20 μM 4-AP. Grey traces show individual trials, and the black bold traces show the averaged responses of five trials. The signal amplitude of fluorescence responses of eEOS was highly variable among synapses. Orange bars represent the timing of stimuli. (**b**) Vesicular release rate (per 20 msec) derived from averaged fluorescence responses of eEOS by deconvolution analysis. (**c**) Cumulative vesicular release. The linear fits (red dashed trace) of slow components of release superimposed on the cumulative vesicular release provide the estimation of N_{RRV}. The N_{RRV} largely varied from synapse to synapse.

According to the quantal model of neurotransmitter release [48–50], it is possible that vesicle release with a single action potential is limited by the finiteness of the number of release sites, at each of which one vesicle at most can be exclusively released at once. I evaluated the number of release sites for a single synapse (N_{site}) by applying a multiple-probability fluctuation analysis based on a binomial model [51–53] to the glutamate imaging data. For this analysis, glutamate signals evoked by a single stimulus were repetitively measured at single synapses under different $[Ca^{2+}]_e$ conditions (Figure 10a), and the mean and variance of the glutamate signals, including failures at each $[Ca^{2+}]_e$ condition, were obtained. The variance showed a bell-shaped dependence on the mean as expected from the binomial model (Figure 10b). The parabolic fit to the variance–mean plot shown in Figure 10 gave an estimate for N_{site} of 2.8; that is, approximately three release sites were present in this synapse. The release probability per release site (P) was 0.23 under normal (2 mM) $[Ca^{2+}]_e$, and P was 0.01, 0.04, 0.14, and 0.51 for $[Ca^{2+}]_e$ of 0.5, 1, 1.5, and 4 mM, respectively, and 0.83 for 4 mM $[Ca^{2+}]_e$ plus 4-AP. The obtained quantal parameters N_{site} and P well accounted for the success rate of glutamate release (Figure 11) as well as the amplitude distribution of glutamate signals (Figure 12).

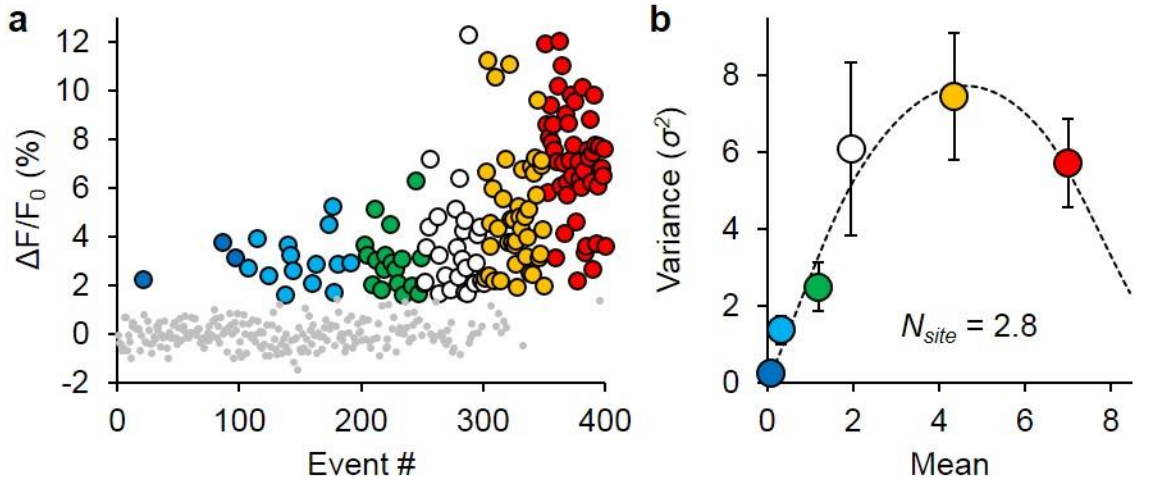

Figure 10 | Estimation of N_{site} by multiple-probability fluctuation analysis at a single synapse. (**a**) The amplitudes of fluorescence responses of eEOS at a synapse evoked by a single stimulus are plotted over time. $[Ca^{2+}]_e$ was varied sequentially: blue, 0.5 mM; cyan, 1 mM; green, 1.5 mM; white, 2 mM; orange, 4 mM; red, 4 mM $[Ca^{2+}]_e$ plus 4-AP. (**b**) Variance–mean plot of fluorescence response of eEOS. The dotted line shows the parabolic fit based on a binomial model of glutamate release. Error bars indicate theoretical estimates of standard errors of the variance using *h*-statistics.

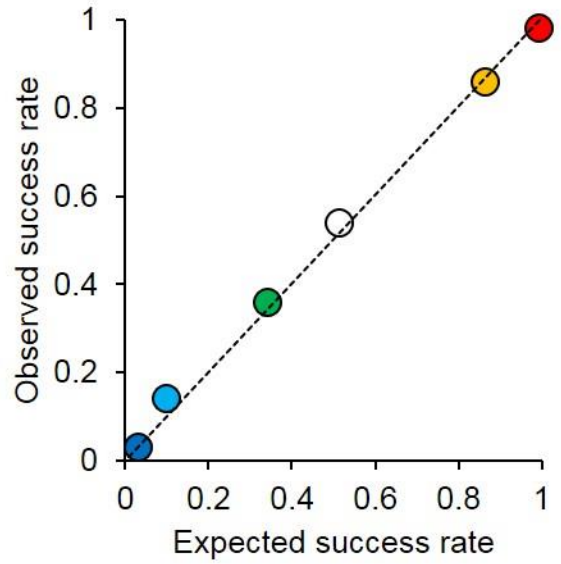

Figure 11 | Estimated quantal parameters account the success rate of glutamate release. Relationship between expected and observed success rates of glutamate release at the same synapse in Figure 10, showing very good agreement between them. The expected success rate is calculated as $1-(1-P)^{N_{site}}$.

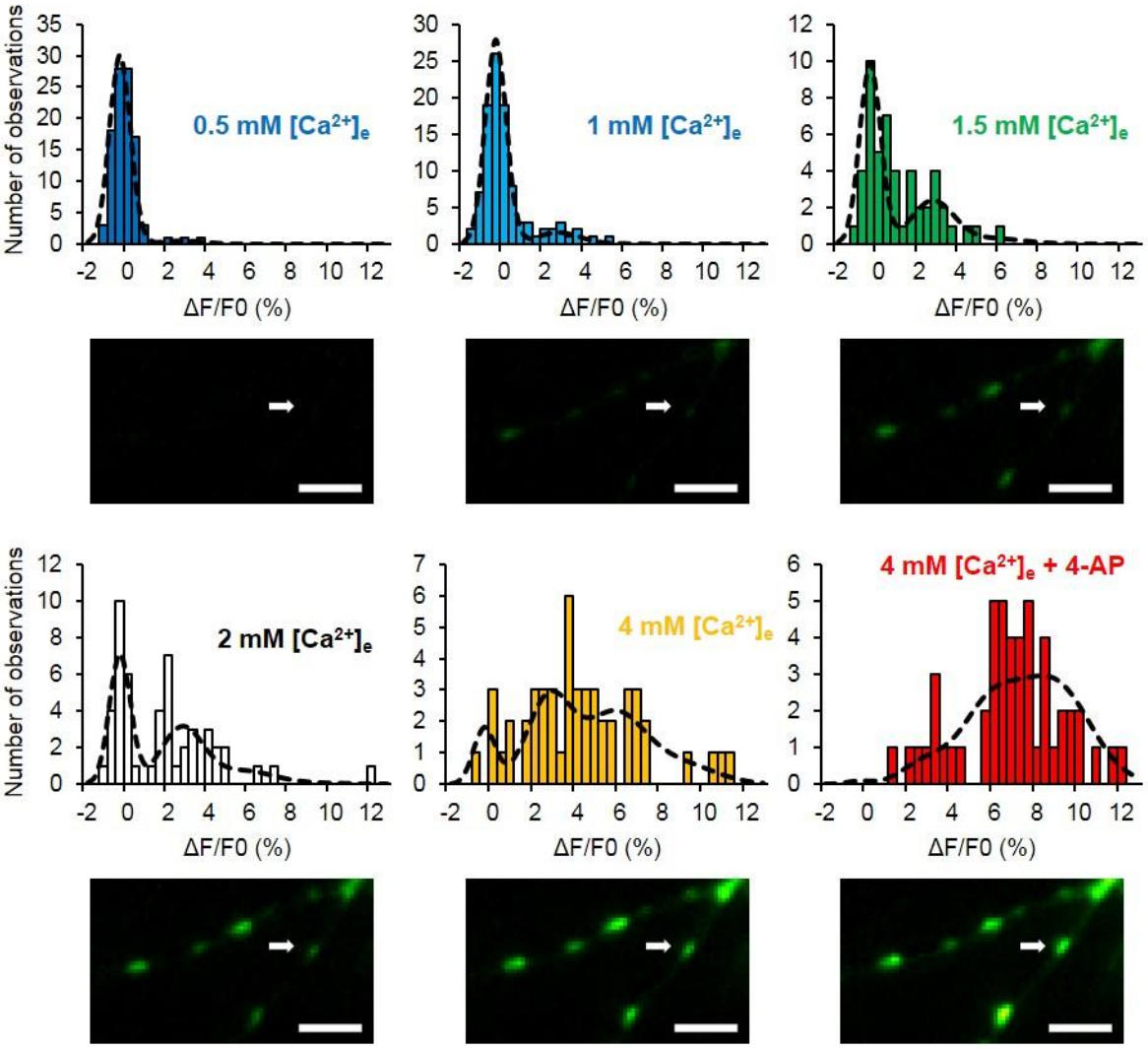

Figure 12 | Estimated quantal parameters account the amplitude distribution of glutamate signals. Histogram analysis of fluorescence responses of eEOS at a single synapse under conditions of multiple release probabilities (related to Figure 10). The color coding is the same as in Figure 10: blue, 0.5 mM (n = 100 events); cyan, 1 mM (n = 100 events); green, 1.5 mM (n = 50 events); white, 2 mM (n = 50 events); orange, 4 mM (n = 50 events); red, 4 mM $[Ca^{2+}]_e$ plus 4-AP (n = 50 events). Dashed lines show binomial release model distributions generated with quantal parameters estimated by multiple-probability fluctuation analysis in Figure 10. N_{site} = 3, Q = 3.1 %, P = 0.01, 0.04, 0.14, 0.23, 0.51, and 0.83, respectively. Background noise standard deviation (SD) of 0.5 % and quantal variability (CV = 0.28) were also taken into account for the distribution. Cramér–von Mises test was used for testing goodness-of-fit. $P > 0.05$ for all conditions. Panels beneath the histograms show corresponding averaged glutamate signal images, and arrows indicate the analyzed synapse.

Multiple-probability fluctuation analysis was successful in 53 out of 71 synapses; 18 synapses did not fulfil the criteria for accurate N_{site} estimation (maximal $P > 0.45$). The N_{site} was highly variable among synapses, distributing between 1 and 18, with an average of 4.9 and a coefficient of variation (CV) of 0.69 (Figure 13). These values indicate that there are multiple release sites in a single presynaptic terminal, and that the presynaptic strength varies widely among synapses. After estimating N_{site}, I also quantified N_{RRV} using a 50 Hz-burst stimulation protocol for the same synapses. The numbers, N_{site} and N_{RRV}, were found to be nearly equivalent in one-to-one correspondence (Figure 13). This equality indicates that all the release sites are occupied by readily releasable vesicles, and that vesicles must be set at the release sites to be readily releasable.

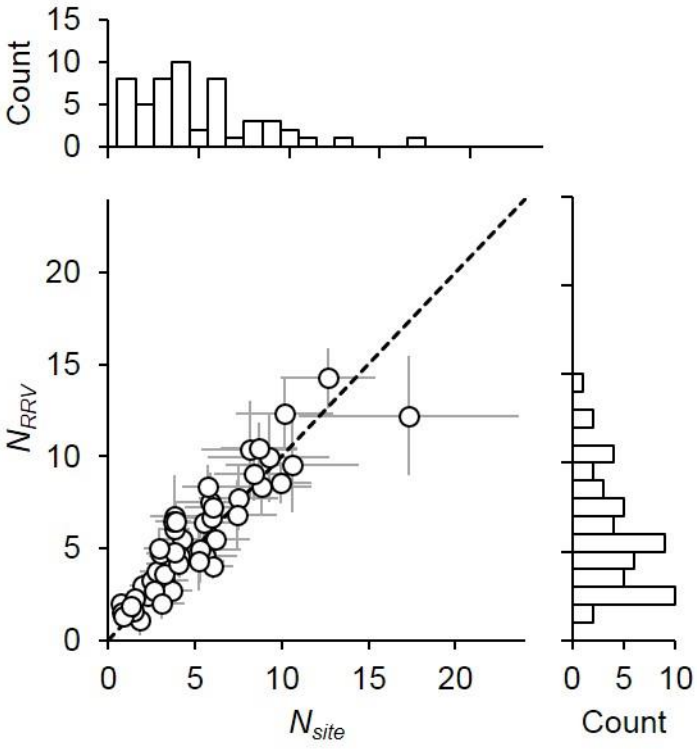

Figure 13 | The number of release sites matches the number of releasable vesicles. Scatter plot and marginal histograms of N_{site} and N_{RRV} among synapses (n = 53 synapses). Bootstrap resampling analysis of binomial fit was performed to evaluate standard errors for N_{site}. N_{RRV} was determined from five trials for all synapses. The dashed line corresponds to equality of these two estimates.

In addition to the variability in N_{RRV} and N_{site}, the above analysis also revealed variability in P among synapses, showing an average of 0.21 with a CV of 0.57 in the normal $[Ca^{2+}]_e$ condition. However, N_{RRV} and P did not appear to be correlated (Figure 14). A plot of N_{RRV} against P for 71 synapses showed a random scatter with no statistical correlation, indicating that the number of release sites is determined independently of the release probability.

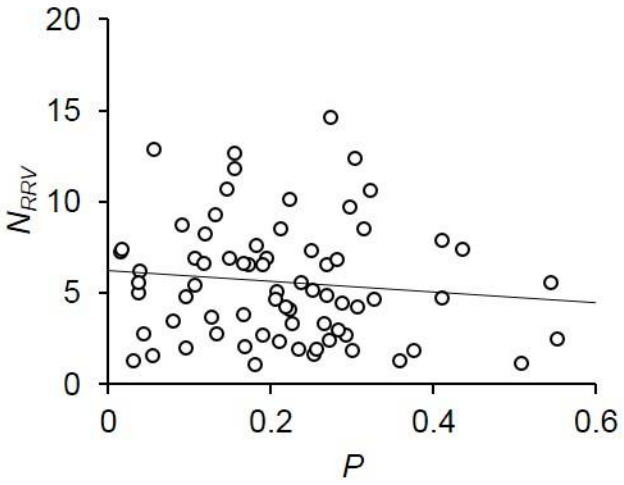

Figure 14 | Relationship between the release probability and the number of releasable vesicles. Scatter plot of the release P and N_{RRV}. There is no significant correlation (Pearson's correlation, R = -0.11, P = 0.36, n = 71 synapses).

Short-term synaptic plasticity is alteration of synaptic efficacy rapidly developing during repetitive activity, the mechanism of which is believed to be mainly presynaptic [64]. Having found the independence of the two presynaptic parameters N_{site} and P, I asked whether these two parameters differentially affect short-term plasticity. I evaluated the number of synaptic vesicles released in response to trains of stimuli at 20 Hz. I found that synapses with higher P showed greater depression during trains of stimuli (Figure 15a). By contrast, N_{site} only scaled the amplitude of vesicular release without affecting the temporal dynamics during the stimulus trains (Figure 15b).

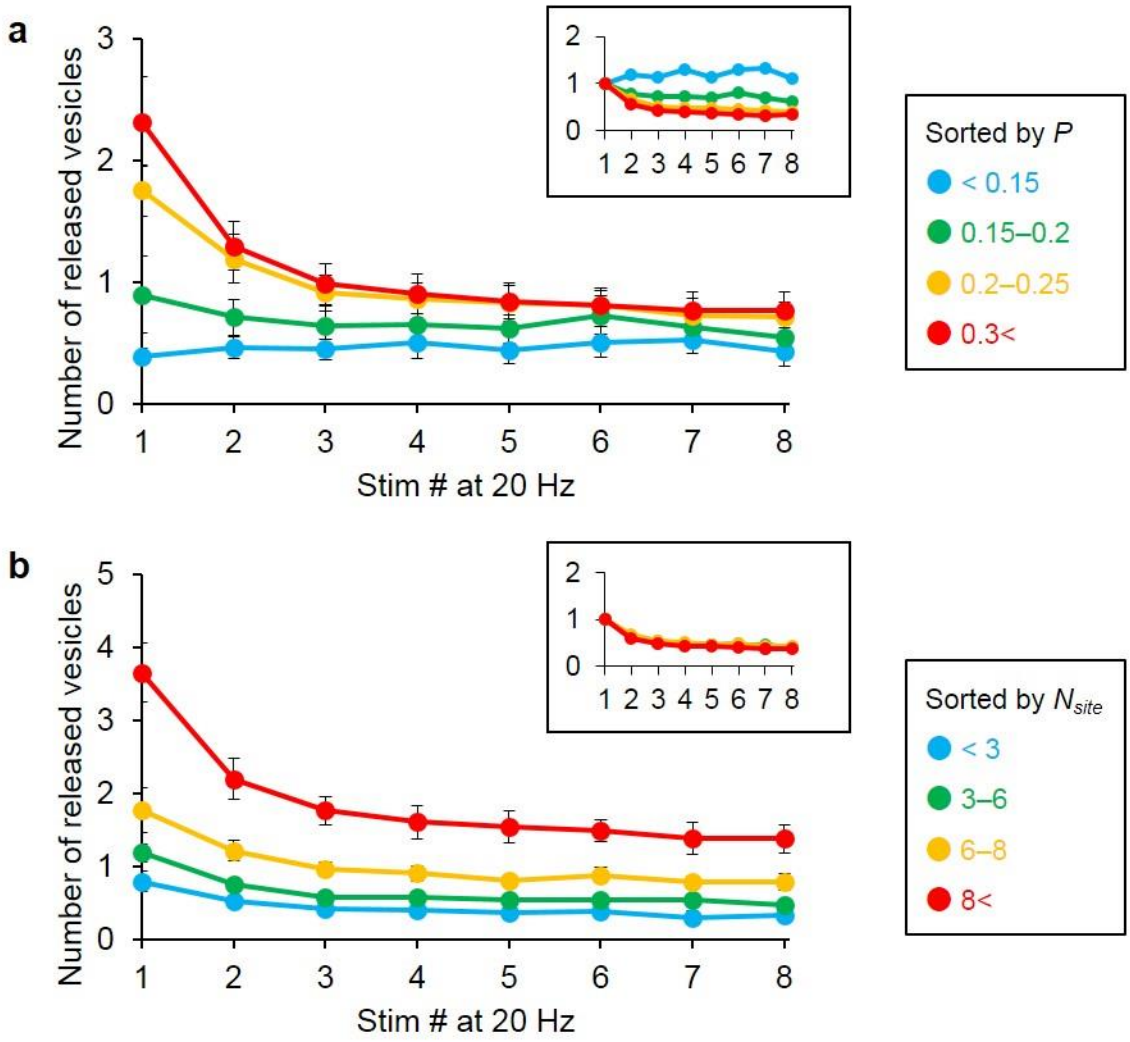

Figure 15 | The release probability, but not the number of release sites, determines the short-term dynamics of glutamate release. (**a**) Averaged vesicular release at single synapses in response to eight stimuli at 20 Hz. Synapses were grouped into four categories relative to P (blue, <0.15, n = 8; green, 0.15–0.2, n = 6; orange, 0.2–0.3, n = 17; red, 0.3<, n = 22). Error bars indicate SEM. Inset depicts the normalized vesicular release. P affects short-term plasticity of vesicular release. Correlation analysis of ungrouped data confirmed the P dependence of the normalized vesicular release for each of successive stimulus (Spearman rank correlation for 2nd to 8th stimuli, R = -0.50, -0.58, -0.57, -0.55, -0.58, -0.72, respectively; $P < 10^{-4}$ for all stimuli, n = 53 synapses). (**b**) Averaged vesicular release at single synapses in response to eight stimuli at 20 Hz. Synapses were grouped into four categories relative to N_{site} (blue, <3, n = 9; green, 3–6, n = 25; orange, 6–8, n = 9; red, 8<, n = 10). Inset depicts the normalized vesicular release. N_{site}, which changes the quantity of vesicular release, does not affect short-term plasticity. Correlation analysis of ungrouped data confirmed the N_{site} independence for each of successive stimulus (Spearman rank correlation for 2nd to 8th stimuli, R = −0.15, −0.10, −0.12, −0.06, −0.004, −0.06, respectively; $P > 0.2$ for all stimuli, n = 53 synapses).

Munc13-1 constitutes the quantal release site

In addressing the mechanism that determines the number of release sites (or releasable vesicles) at individual synapses, I focused on Munc13-1 because of its predominant localization in the AZ [33, 35] and its essential role in synaptic transmission [29–32]. I estimated the number of Munc13-1 molecules at synapses using direct immunofluorescence with an intensity-calibrated Alexa-647 labeled Munc13-1 monoclonal antibody (Figure 16). The estimated number of Munc13-1 molecules was on average 54 per synapse (n = 123), varying among synapses with a CV of 0.63. This CV value was similar to that for N_{RRV} (Figure 13).

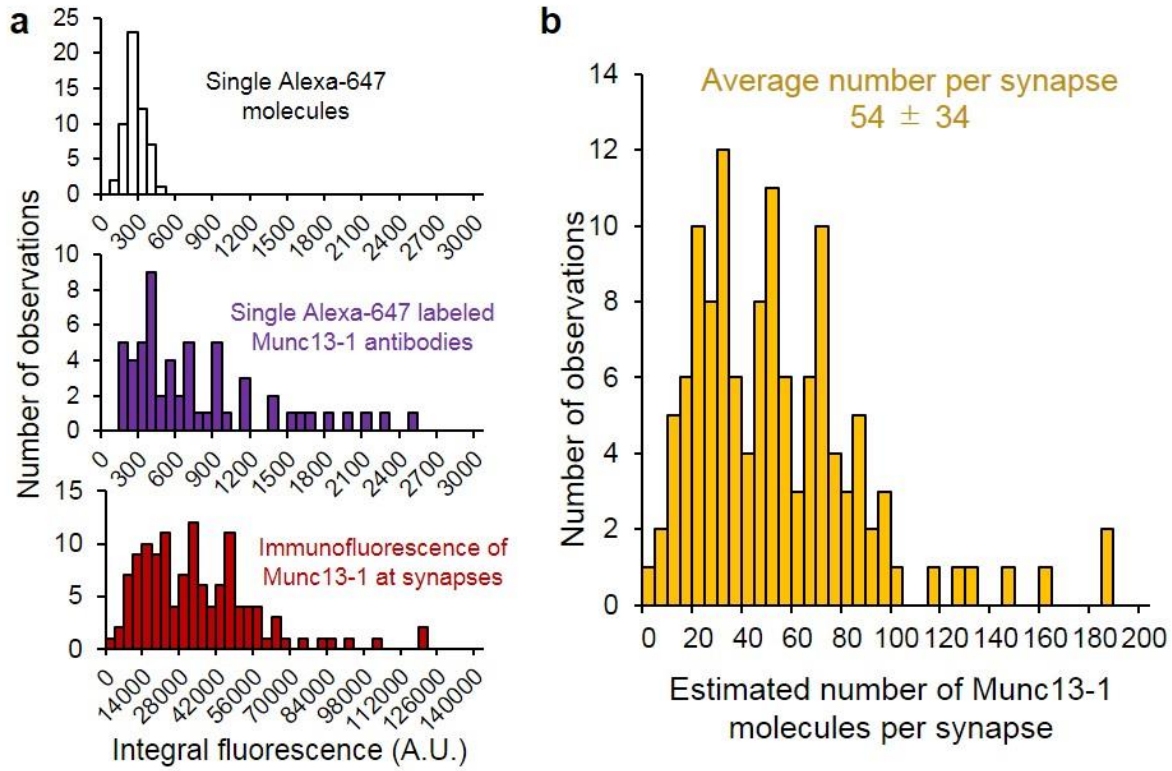

Figure 16 | Quantification of Munc13-1 molecules at synapses. (**a**) Histogram of integral fluorescence of single Alexa-647 molecules (top), single Alexa-647 labeled monoclonal antibodies (middle), and single synapse Munc13-1 immunofluorescence (bottom). (**b**) Histogram of estimated number of Munc13-1 molecules (binding antibodies) among synapses. Estimations were carried out by immunofluorescence calibration using Alexa-647 labeled Munc13-1 monoclonal antibody.

Then, I performed immunostaining after glutamate imaging to examine the relationship between the amount of Munc13-1 and glutamate release at individual synapses (Figure 17). The quantitative analysis showed that the number of Munc13-1 molecules per synapse was significantly correlated with N_{RRV}, but not with P (Figure 18).

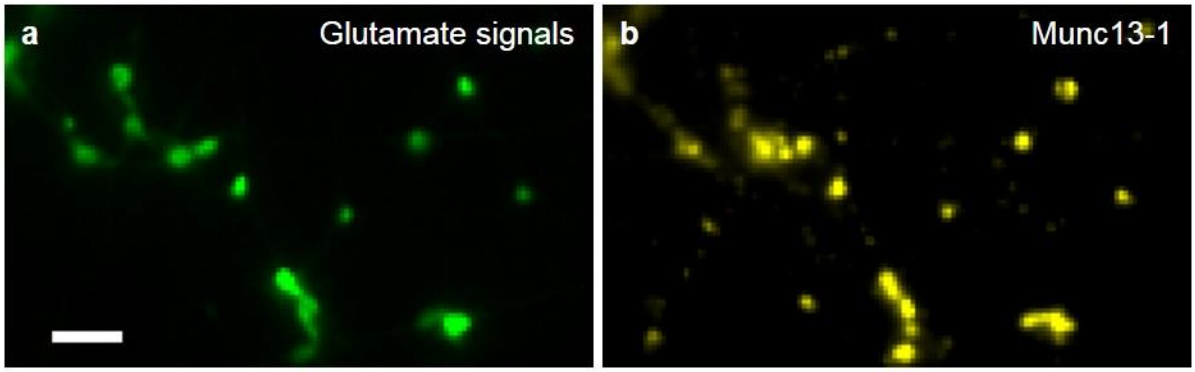

Figure 17 | Post-hoc immunocytochemistry of Munc13-1 after glutamate imaging. (**a**, **b**) Images of fluorescence responses of eEOS in response to a single stimulus at 4 mM $[Ca^{2+}]_e$ plus 4-AP (**a**) and the corresponding immunofluorescence of Munc13-1 (**b**). Under such high release probability conditions, the spatial correlation between these two images is high. Scale bar, 5 µm.

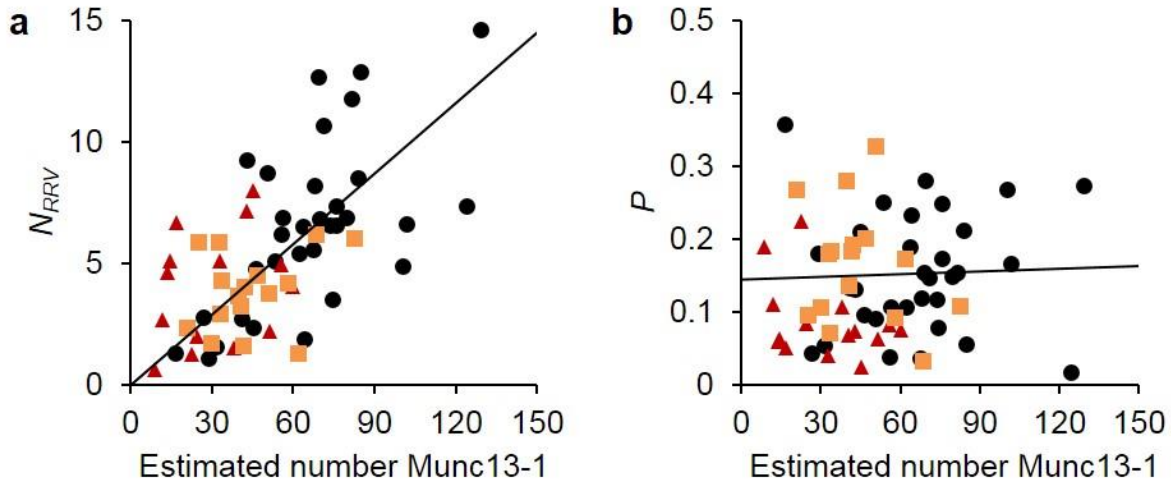

Figure 18 | Munc13-1 determines the number of quantal release sites at individual synapses. (**a**, **b**) Relationships between the number of Munc13-1 molecules and N_{RRV} (**a**) and P (**b**) at individual synapses, respectively. There is a positive correlation for N_{RRV} (Pearson's correlation, $R = 0.61$, $P = 0.00019$) but no correlation for P ($R = 0.037$, $P = 0.84$). The line approximations are derived from control synapse data. Black circles, control ($n = 32$ synapses from); red triangles, Munc13-1 knockdown ($n = 15$ synapses); orange squares, RIM1 knockdown ($n = 16$ synapses).

To test the causative role of Munc13-1 abundance, I manipulated the amount of Munc13-1 using short-hairpin RNA (shRNA). The shRNA against Munc13-1 achieved strong (~90%) knockdown of Munc13-1 without changing the expression of other AZ proteins (Figure 19). Glutamate release was almost completely abolished (4.1% of control, $n = 60$), consistent with

the results of Munc13-1 knockout mice [29–32].

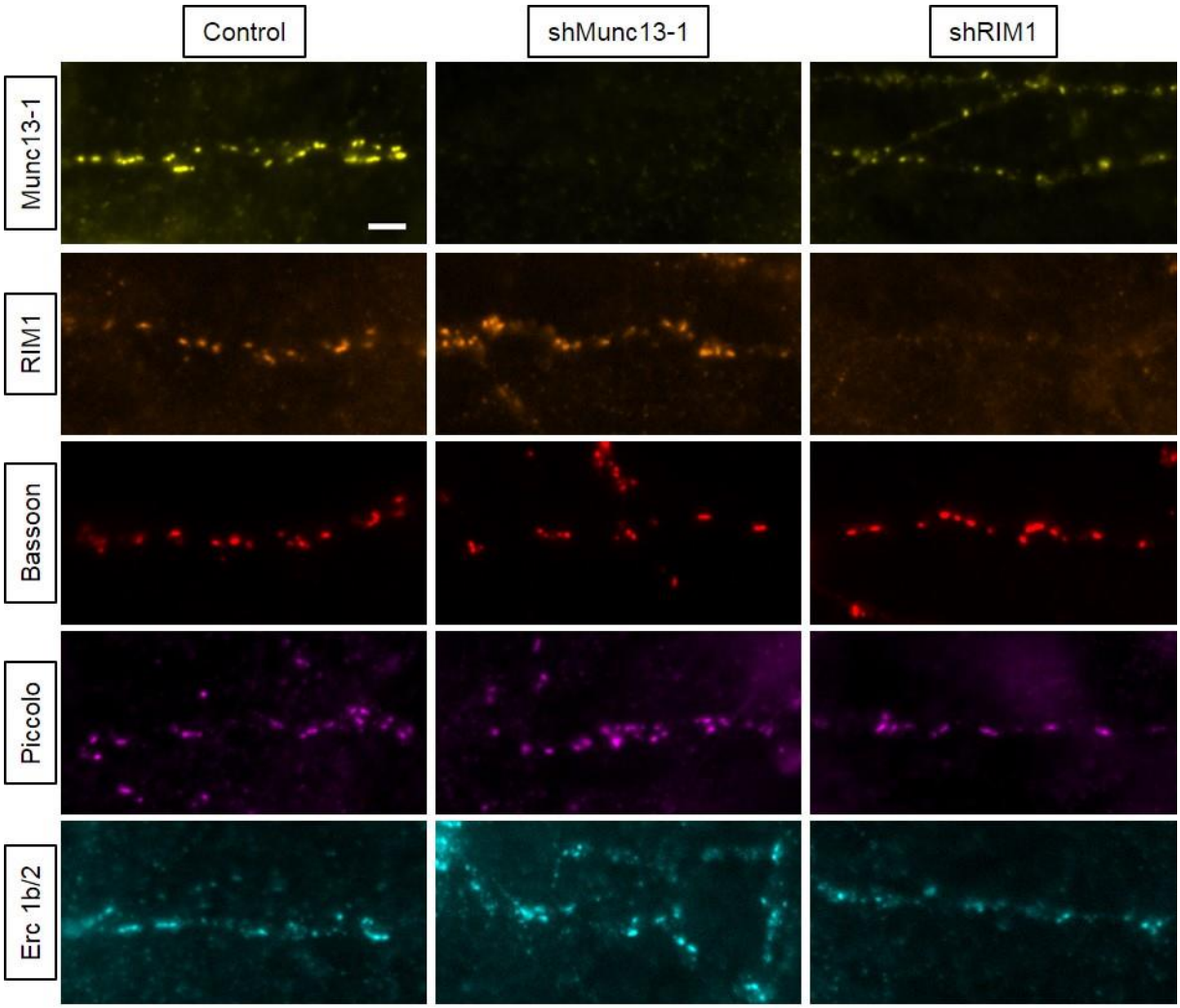

Figure 19 | Immunocytochemical analysis of AZ proteins in Munc13-1 or RIM1 knockdown synapses. Representative immunofluorescence images of major AZ proteins, including Munc13-1, RIM1, bassoon, piccolo, and ERC1b/2, in control, Munc13-1 shRNA lentivirus-infected neurons and RIM1 shRNA lentivirus-infected neurons. Scale bar, 5 μm.

Because this severe knockdown precludes any further estimation of changes in synaptic parameters, I next analyzed glutamate release in synapses with a milder knockdown by using lower levels of shRNA transduction. I also manipulated the amount of Munc13-1 by knockdown of RIM1 (Figure 19), as AZ recruitment of Munc13-1 is RIM-dependent [65]. N_{RRV}

was decreased concomitantly with the decreased levels of Munc13-1 for both of these manipulations (Figure 18a and Figure 20). This result indicates a causative relationship between the amount of Munc13-1 and the number of release sites in synapses.

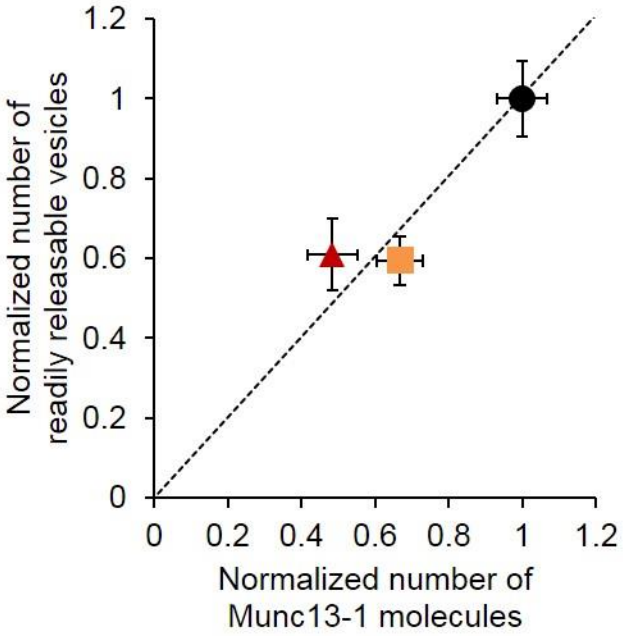

Figure 20 | Munc13-1 determines the number of releasable vesicles at individual synapses. Relation between number of Munc13-1 molecules per synapse and the number of readily releasable vesicles. Concomitant reductions in the number of Munc13-1 molecules and N_{RRV} are observed with genetic manipulations of Munc13-1 levels. The data shown in Figure 18 are used for replotting. Error bars indicate SEM.

To obtain insight into the relationship between Munc13-1 and the quantal release site organization, I studied the supramolecular architecture of Munc13-1 by using 3D-STORM. In conventional diffraction-limited fluorescence microscopic images, Munc13-1 fluorescence appeared blurred at synapses, providing no discernible subsynaptic structures (Figure 21a). By contrast, 3D-STORM images revealed nanoscale discrete spots of Munc13-1 at the subsynaptic level (Figure 21b). Similar discrete nanostructures of Munc13-1 were observed using another monoclonal antibody (Figure 22). The observed discrete structure was not an artefact attributable to undersampling caused by sparse antibody staining (Figure 23) or insufficient

data acquisition (Figure 24). Therefore, Munc13-1 should form sub-synaptic the nanoscale discrete structures. I here term it “Munc13-1 nanoassembly”.

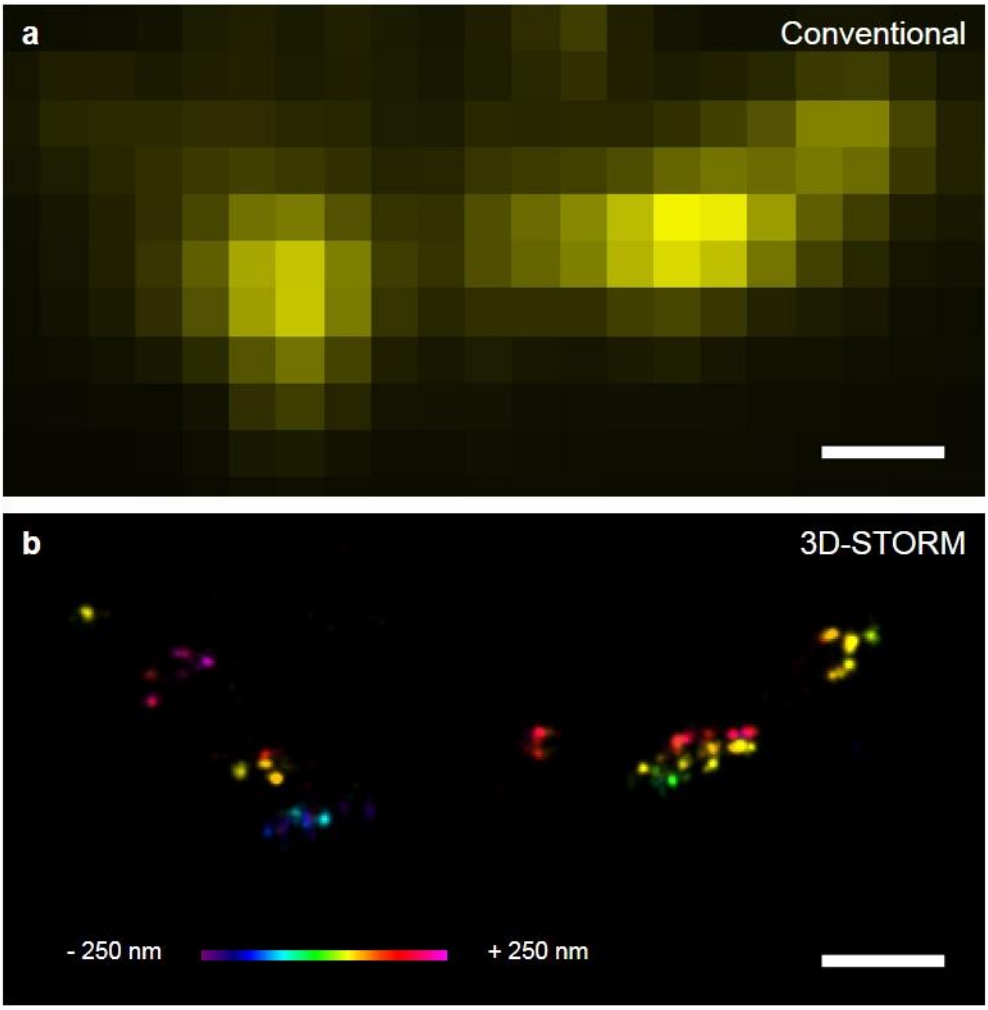

Figure 21 | 3D-STORM imaging of Munc13-1 at synapses. (**a**, **b**) Conventional microscopy image (**a**) and a 3D-STORM image (**b**) of Munc13-1 immunostained with a Munc13-1 monoclonal antibody (clone: 11B-10G) and Alexa Fluor 647-labeled secondary antibody. Scale bars, 500 nm. In 3D-STORM images, the z-positions are color-coded according to the colored scale bar.

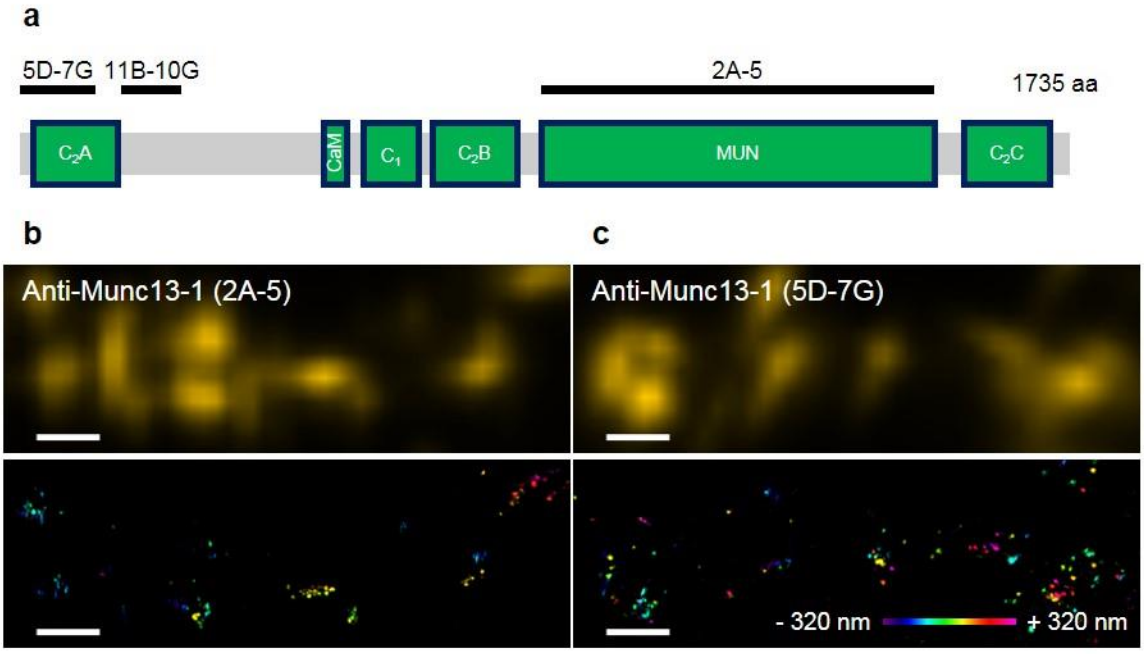

Figure 22 | 3D-STORM imaging of Munc13-1 using monoclonal antibodies. (**a**) A domain structure of Munc13-1 and epitope sites for the Munc13-1 monoclonal antibodies used in this study are shown. (**b, c**) Conventional microscopy images (top) and 3D-STORM images (bottom) of Munc13-1 immunostaining with monoclonal antibodies 2A-5 (**b**) and 5D-7G (**c**). Scale bars, 1 μm. The z-positions are color-coded.

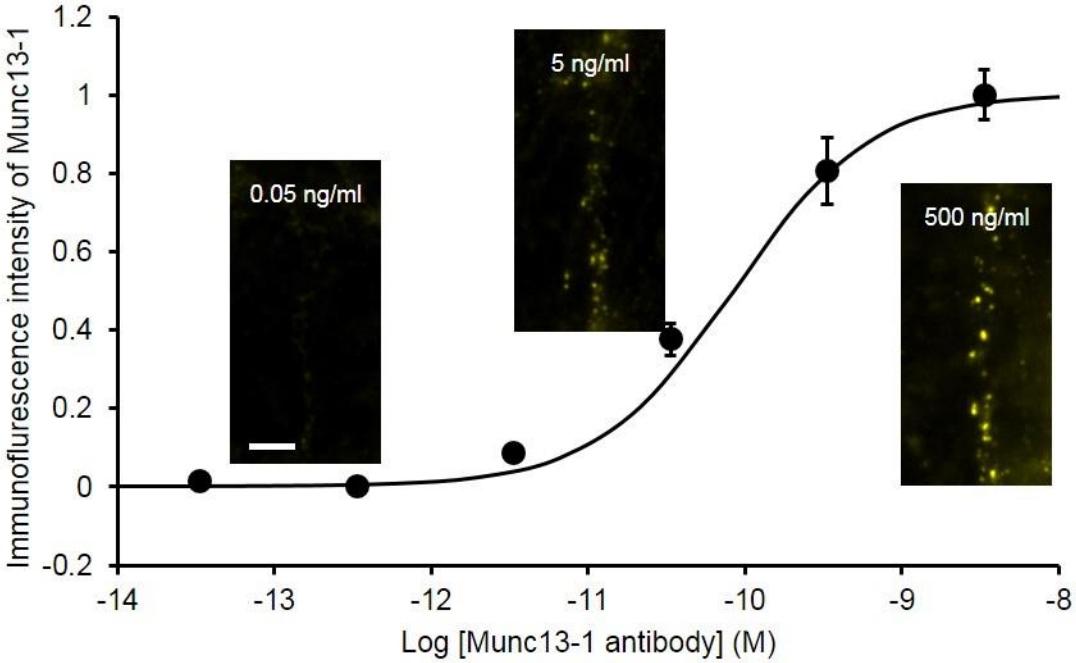

Figure 23 | Optimization of antibody concentration for staining synaptic Munc13-1. Titration curve of Munc13-1 monoclonal antibody (clone: 11B-10G) for staining of synaptic Munc13-1. Each data point results from 60–120 synapses. Data shown are mean ± SEM. Practical experiments were performed at 500 ng/mL (a concentration at which most epitopes are saturated with primary antibodies).

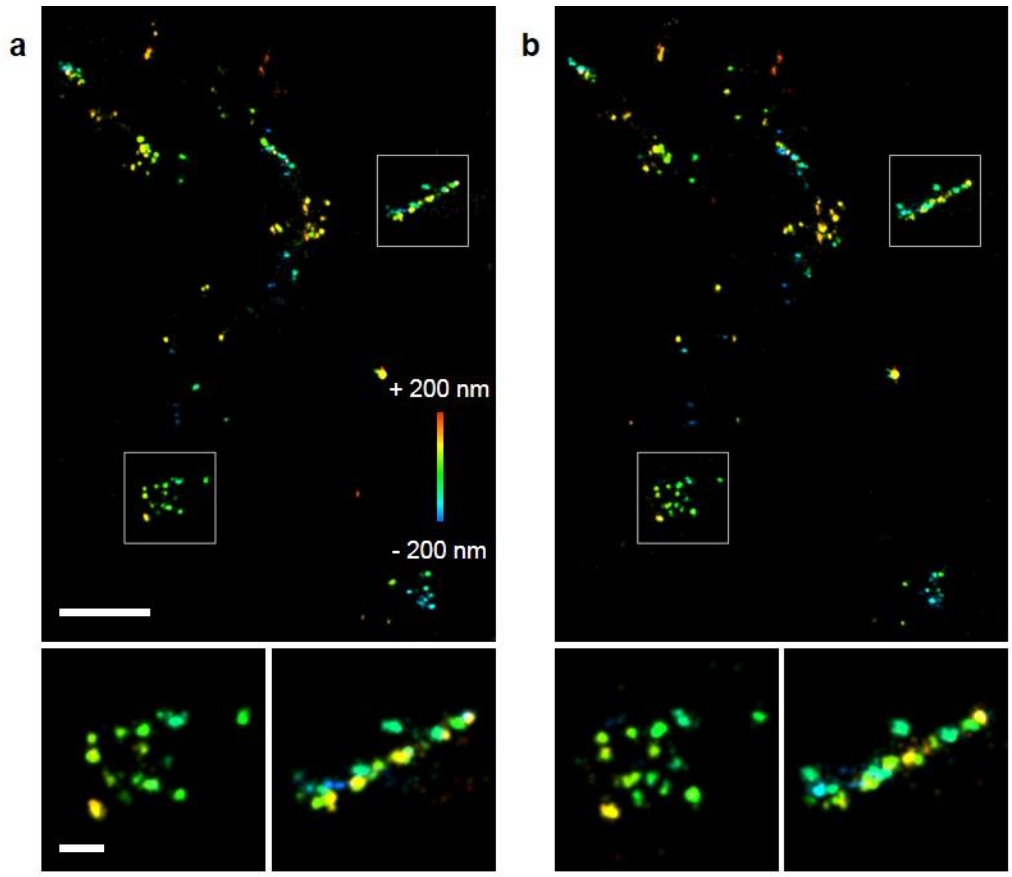

Figure 24 | Reproducibility of nano-structures in 3D-STORM imaging. (**a**, **b**) 3D-STORM images of Munc13-1 immunostained with monoclonal Munc13-1 antibody and Alexa-647 labeled secondary antibody. Images reconstructed from the initial 25,000 frames of data acquisition (**a**) and from the subsequent 25,000 frames of data acquisition (**b**) are shown. Bottom row of images shows enlarged view of the white-boxed region in the top panels. Scale bars, 2 μm (top) and 200 nm (bottom). The z-positions are color-coded.

I performed 3D-rotation of STORM images and obtained their 2D-projections on the AZ surface to analyze the geometric features of Munc13-1 nanoassemblies at the AZ (Figure 25). The diameter of individual Munc13-1 nanoassemblies measured in full width at half maximum was 44.9 ± 12.0 nm. The center-to-center distance between nearest neighboring assemblies was 84.7 ± 22.7 nm. The small variations in the size and in inter-assembly distance indicate an ordered organization of Munc13-1 in the AZ. This indication is consistent with a previous

electron microscopy study showing that Munc13-1 resides between dense projections [35]. Furthermore, pair-correlation analysis of Munc13-1 STORM data points revealed oscillatory distribution with a positive clustering within 50 nm and negative clustering in a range of 50 to 100 nm (Figure 26).

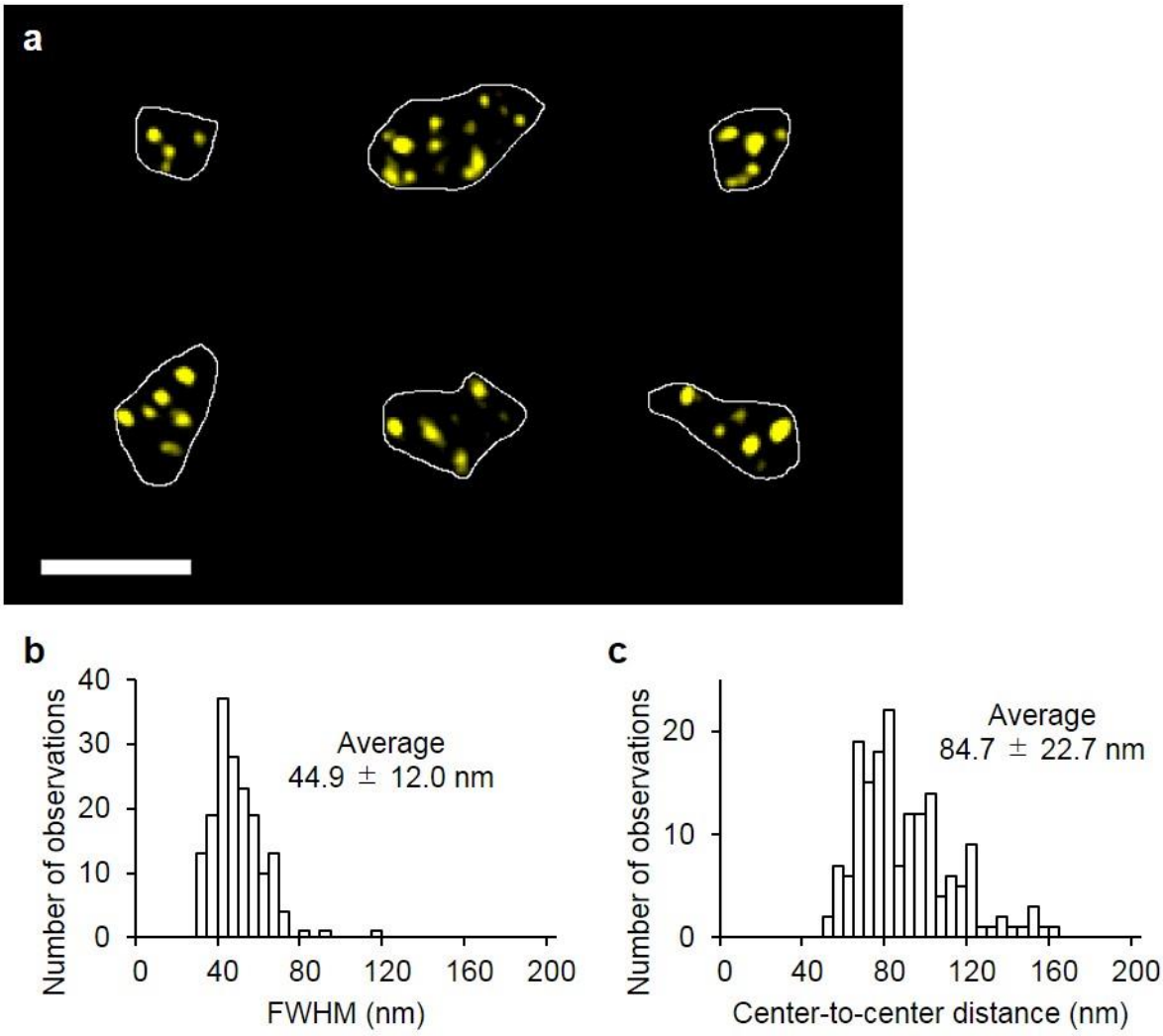

Figure 25 | Distribution of Munc13-1 nanoassemblies within the AZ. (**a**) Munc13-1 nanoassemblies superimposed on AZ surfaces estimated with 3D rotation of STORM images. Scale bar, 500 nm. (**b**, **c**) Histogram of the full width at half maximum (**b**) and the center-to-center distance between nearest neighboring (**c**) of Munc13-1 nanoassemblies. In total, 169 nanoassemblies were analyzed (mean ± SD).

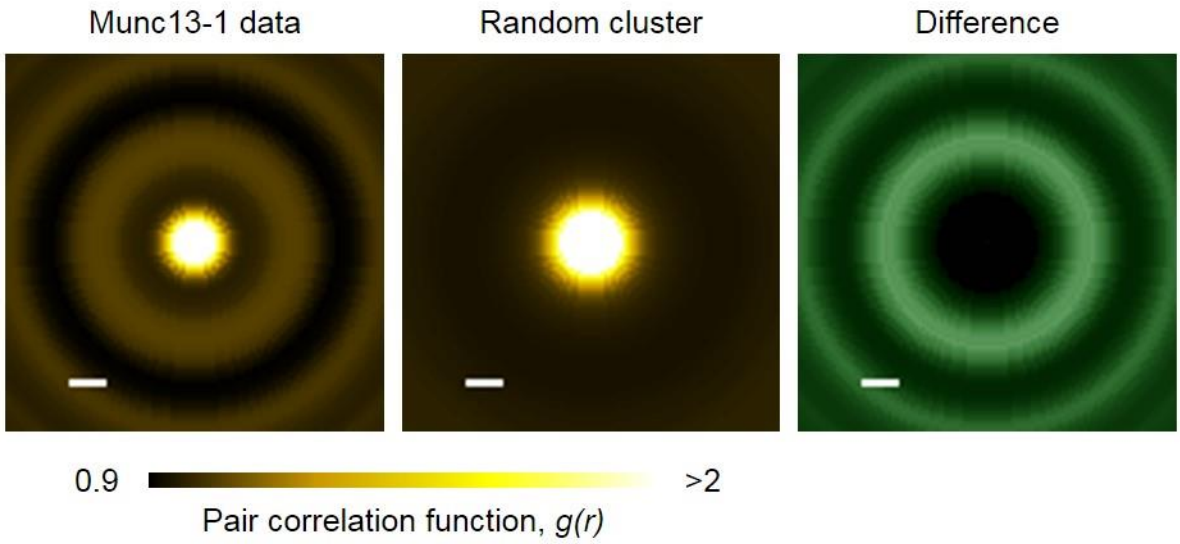

Figure 26 | Pair-correlation analysis of Munc13-1 molecules in the AZ. 2D map of pair-correlation function *g(r)* of Munc13-1 STORM data (left, data from 169 Munc13-1 nanoassemblies) and of simulation data of random cluster distribution (middle). Right panel shows the difference between *g(r)* of Munc13-1 STORM data and of random cluster simulation data. Scale bars, 50 nm. The analysis shows oscillatory distribution of Munc13-1 molecules in the AZ surface: positive clustering within 50 nm, negative clustering at 50–100 nm, positive clustering at 100–160 nm, and negative clustering at 160–235 nm. The highly positive clustering at ~50 nm may represent not only clustering of Munc13-1 molecules but also over-counting due to multiple Alexa Fluor 647 switching and multiple dye labeling.

The average number of Munc13-1 nanoassemblies at the AZ was 5.7 ± 3.6 (Figure 27); each nanoassembly hence consists of at least nine Munc13-1 molecules based on the estimated number of molecules (binding antibodies) per synapse (Figure 16). I note that the number of Munc13-1 nanoassemblies is similar to the value for N_{RRV}. To directly verify the correlation, I quantified the number of Munc13-1 nanoassemblies in synapses at which N_{site} and N_{RRV} were determined by glutamate imaging. I found that the number of Munc13-1 nanoassemblies closely matched N_{site} and N_{RRV} at the same individual synapses (Figure 28). Based on this equivalence, I hypothesize that the Munc13-1 nanoassembly is the physical entity of the quantal release site.

Consistent with this hypothesis, the reduction in N_{RRV} in RIM1 knockdown synapses (Figure 20) was comparable to the reduction in the number of Munc13-1 nanoassemblies at the AZ (Figure 27).

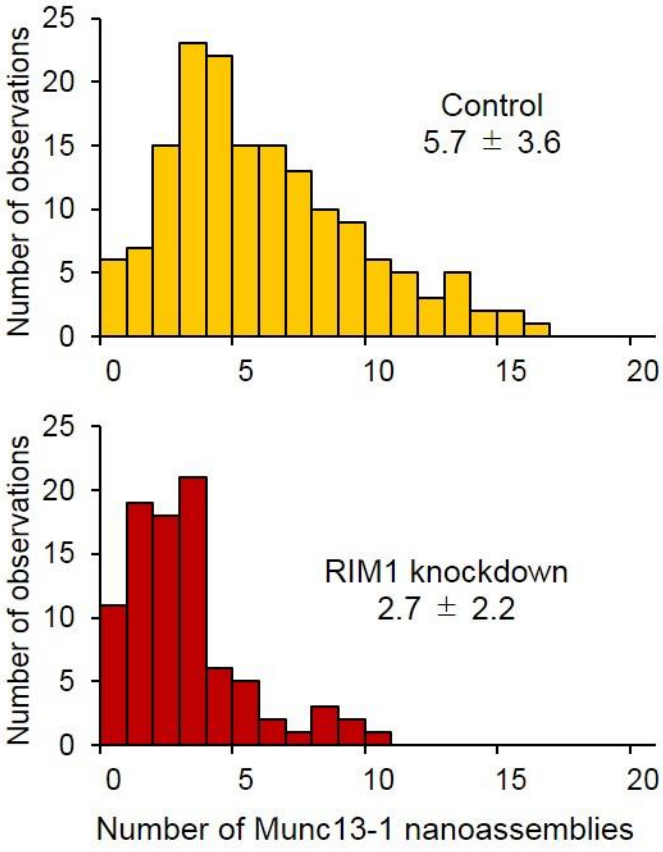

Figure 27 | Number of Munc13-1 nanoassemblies at AZs. Histogram of the number of Munc13-1 nanoassemblies in control (upper panel; 5.7 ± 3.6, mean ± SD, n = 159 AZs) and RIM1 knockdown (lower panel; 2.7 ± 2.2, mean ± SD, n = 89 AZs) neurons. The number of Munc13-1 nanoassemblies was smaller in RIM1 knockdown neurons (Wilcoxon rank sum test, $P = 1.2 \times 10^{-12}$).

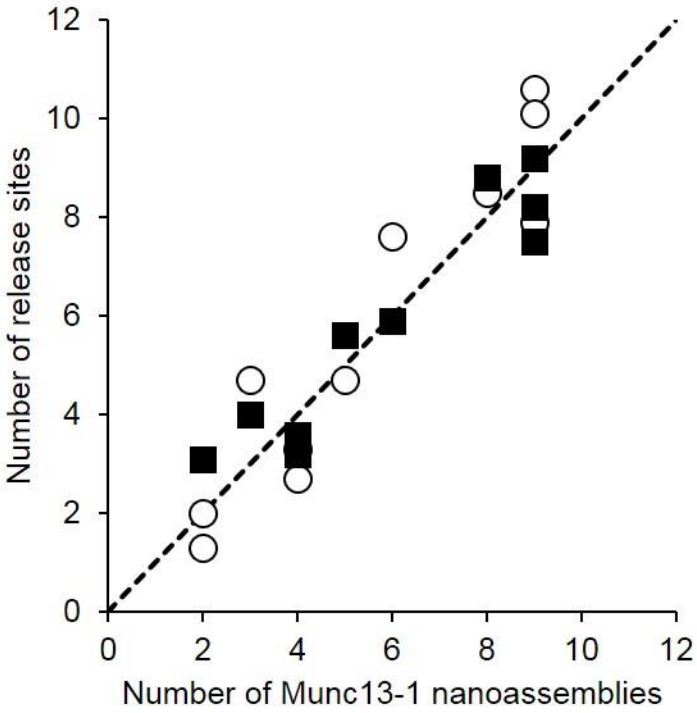

Figure 28 | Munc13-1 nanoassembly corresponds to the quantal release site. Relationship between the number of Munc13-1 nano-assemblies and N_{site} (black squares, n = 10 AZs) or N_{RRV} (white circles, n = 11 AZs) at individual synapses. The dashed line corresponds to equality of the two estimates.

Munc13-1 recruits syntaxin-1 at the AZ

If synaptic vesicle exocytosis occurs at the site where Munc13-1 is assembled, exocytosis machinery must be co-assembled with it. To test this prediction, I visualized synaptic syntaxin-1, a core component of the SNARE complex essential for synaptic vesicle exocytosis [66], by optimizing fixation protocols (Figure 29). Then, I analyzed the spatial relationship between Munc13-1 and syntaxin-1 by 3D-STORM imaging, showing an enrichment of syntaxin-1 in the AZ and preferential localization of syntaxin-1 with the Munc13-1 nanoassembly (Figure 30). Pair-correlation analysis of dual-color STORM data further showed nanoscale co-clustering of syntaxin-1 and Munc13-1 (Figure 31).

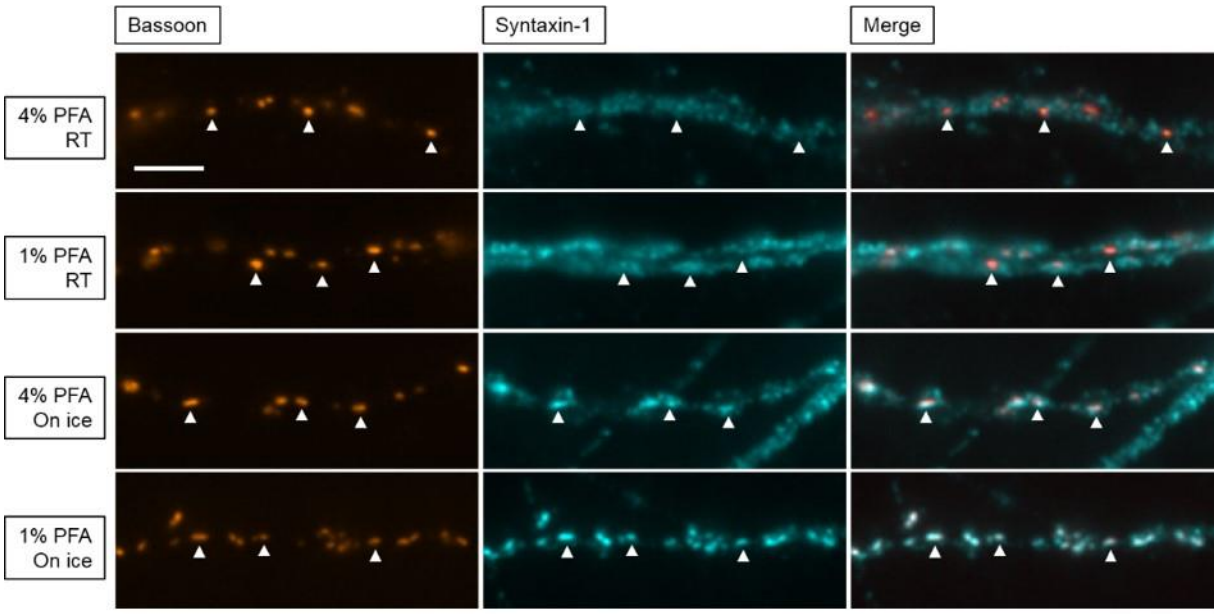

Figure 29 | Optimization of fixation conditions for visualization of synaptic syntaxin-1. Immunofluorecence images of bassoon (orange) and syntaxin-1 (cyan) in various fixation conditions. Cultured hippocampal neurons were fixed with 4% PFA or 1% PFA at RT or on ice. Scale bar, 10 μm. Arrowheads indicate synaptic sites identified by bassoon immunofluorescence. Strong fixation led to dim or negative labeling of syntaxin-1 at synapses

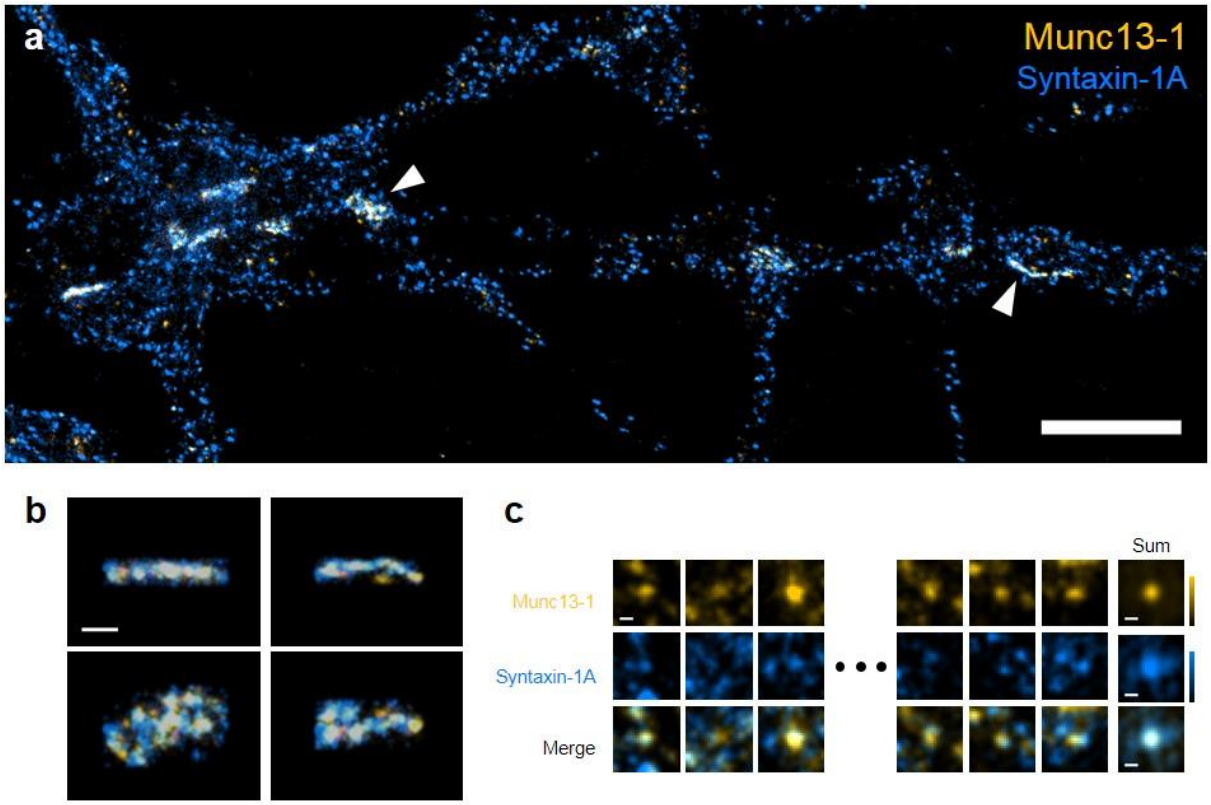

Figure 30 | Munc13-1 and syntaxin-1 assemble at the AZ. (**a**) Dual-color STORM images of Munc13-1 (yellow) and syntaxin-1A (blue) immunostained with Alexa-647/405 and 647/488 labeled secondary antibodies, respectively. Scale bar, 2 µm. (**b**) Side views (top row) and face views (bottom row) of Munc13-1 and syntaxin-1A in AZs indicated by arrowheads in **a**. Scale bar, 200 nm. (**c**) Image-based nanoscale co-localization analysis of Munc13-1 and syntaxin-1A. For this analysis, the centroids of individual Munc13-1 nanoassemblies were locked, and then the Munc13-1 and corresponding syntaxin-1A images were averaged over all images (n = 254 nanoassemblies), respectively. Scale bars, 100 nm.

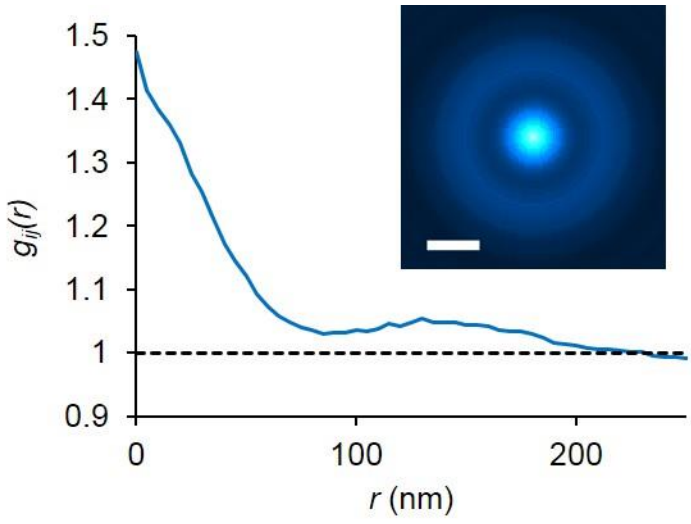

Figure 31 | Pair-correlation analysis of Munc13-1 and syntaxin-1 in the AZ. Marked pair-correlation function *gij(r)* between Munc13-1 and syntaxin-1A 3D-STORM datasets. Pair-correlation values above 1 suggest positive clustering between these two molecules. Right panel shows 2D map of *gij(r)*. Scale bar, 100 nm.

I then examined whether knockdown of Munc13-1 affects syntaxin-1 localization. Notably, whereas overall syntaxin-1 expression was nearly unchanged, as previously reported in Munc13-1 knockout neurons [29, 32], synaptic accumulations of syntaxin-1 were suppressed (Figure 32). Furthermore, 3D-STORM analysis revealed that localized fractions of syntaxin-1 in the AZ were selectively reduced in Munc13-1 knockdown synapses (Figure 33). These results reveal a crucial role of Munc13-1 in recruitment of syntaxin-1 to the AZ. Thus, I hypothesize that Munc13-1 supramolecular assemblies formed at the AZ serve as functional release sites by recruiting syntaxin-1.

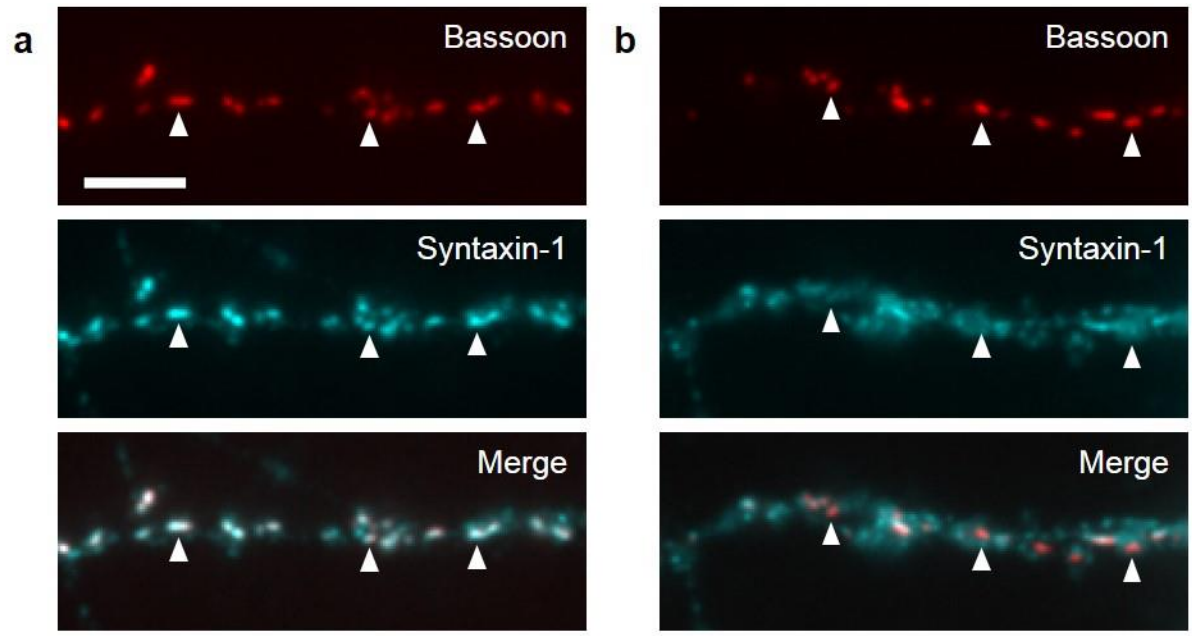

Figure 32 | Reduced localizations of syntaxin-1 at Munc13-1 knockdown synapses. (**a, b**) Immunofluorescence images of bassoon (red) and syntaxin-1 (cyan) of control (**a**) and Munc13-1 knockdown neurons (**b**). Scale bar, 5 μm. Cells were fixed with 1% PFA on ice and permeabilized with saponin. Arrowheads indicate synaptic sites identified by bassoon. Synaptic syntaxin-1 immunofluorescence was clearly observed in control synapses, whereas it was dim in some Munc13-1 knockdown synapses.

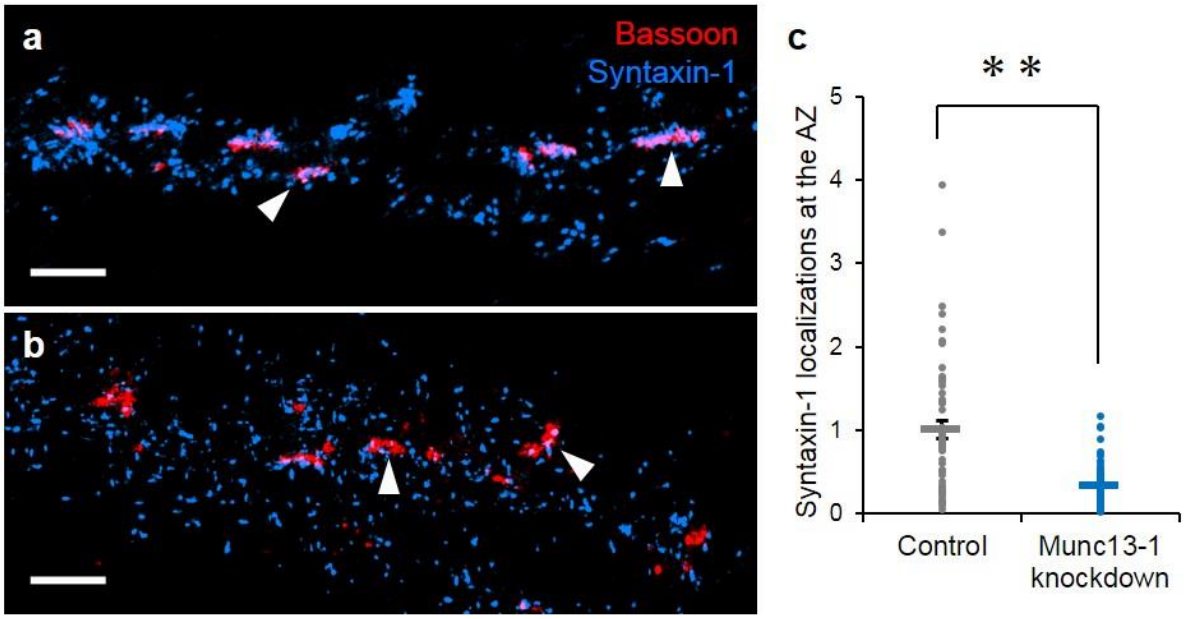

Figure 33 | Reduced localizations of syntaxin-1 at Munc13-1 knockdown AZs. (**a**, **b**) STORM images of bassoon (red) and syntaxin-1 (blue) in control (**a**) and Munc13-1 knockdown neurons (**b**). Bassoon and syntaxin-1 were immunostained with DyLight 755 and Alexa-647 labeled secondary antibodies, respectively. Arrowheads indicated representative AZs. Scale bars, 1 μm. (**c**) Quantification of syntaxin-1 localizations in the AZ of control (n = 58 AZs) and of Munc13-1 knockdown neurons (n = 71 AZs). Error bars indicate SEM. $^{**}P < 0.001$ (Wilcoxon rank sum test).

Reconstitution of release site supramolecular assemblies

I then asked whether formation of the supramolecular assembly of Munc13-1 depends on a particular molecular context of presynaptic terminals in which various presynaptic proteins are localized. I expressed recombinant Munc13-1 in non-neuronal cell lines (293T or COS7). When expressed alone, Munc13-1 was distributed diffusely in the cytosol (Figure 34). To restore the membrane localization of Munc13-1, I designed the artificial membrane anchoring protein ZF-CAAX, which consisted of the zinc-finger domain of RIM1 and a CAAX prenylation motif sequence, expecting to target Munc13-1 to the cell membrane via binding to the N-terminal

C_2A domain of Munc13-1 [65, 67]. When co-expressed with ZF-CAAX, Munc13-1 was translocated to the cell membrane and formed discrete supramolecular self-assemblies (Figure 35). A STORM analysis showed nanoscale structures of Munc13-1 within the reconstituted assemblies (Figure 36) resembling the Munc13-1 nanoassembly as seen in the AZ. The self-assembly was also observed when Munc13-1 was directly translocated to the cell membrane by the application of a phorbol ester (Figure 34). I found that syntaxin-1 was recruited to the reconstituted Munc13-1 supramolecular self-assembly when co-expressed with Munc18-1, a syntaxin-1 binding protein also essential for synaptic vesicle exocytosis [66] (Figure 37). Notably, dual-color STORM images allowed for the visualization of nanoscale recruitments of syntaxin-1 to the Munc13-1 supramolecular self-assembly (Figure 38), as seen at the synaptic vesicle release site in the AZ.

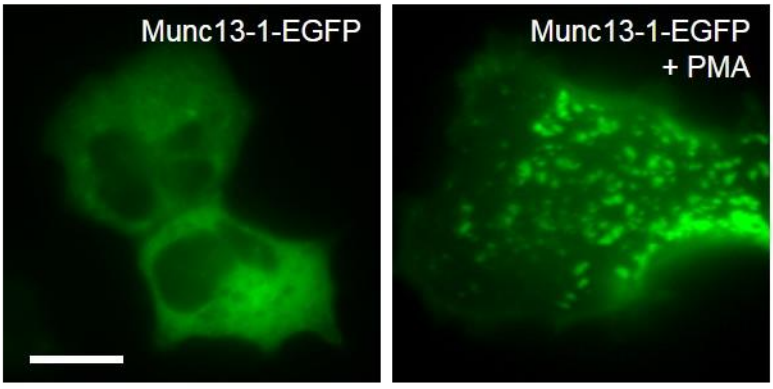

Figure 34 | Overexpression of Munc13-1 in non-neuronal cells. Fluorescence images of Munc13-1-EGFP expressed in 293T cells in the absence (left) or presence (right) of a phorbol ester, PMA. Munc13-1 molecules were translocated to the cell membrane and formed macromolecular self-assemblies with PMA application. Scale bar, 10 μm.

Figure 35 | Reconstitution of Munc13-1 macromolecular assemblies in non-neuronal cells. Fluorescence images of Munc13-1-EGFP (left) and TagRFP-ZF-CAAX (middle) co-expressed in a 293T cell. Right panel shows a merged image. Munc13-1-EGFP and TagRFP-ZF-CAAX form macromolecular self-assemblies at the cell membrane. TagRFP-ZF-CAAX expression alone does not form macromolecular assemblies (data not shown). Scale bar, 10 µm.

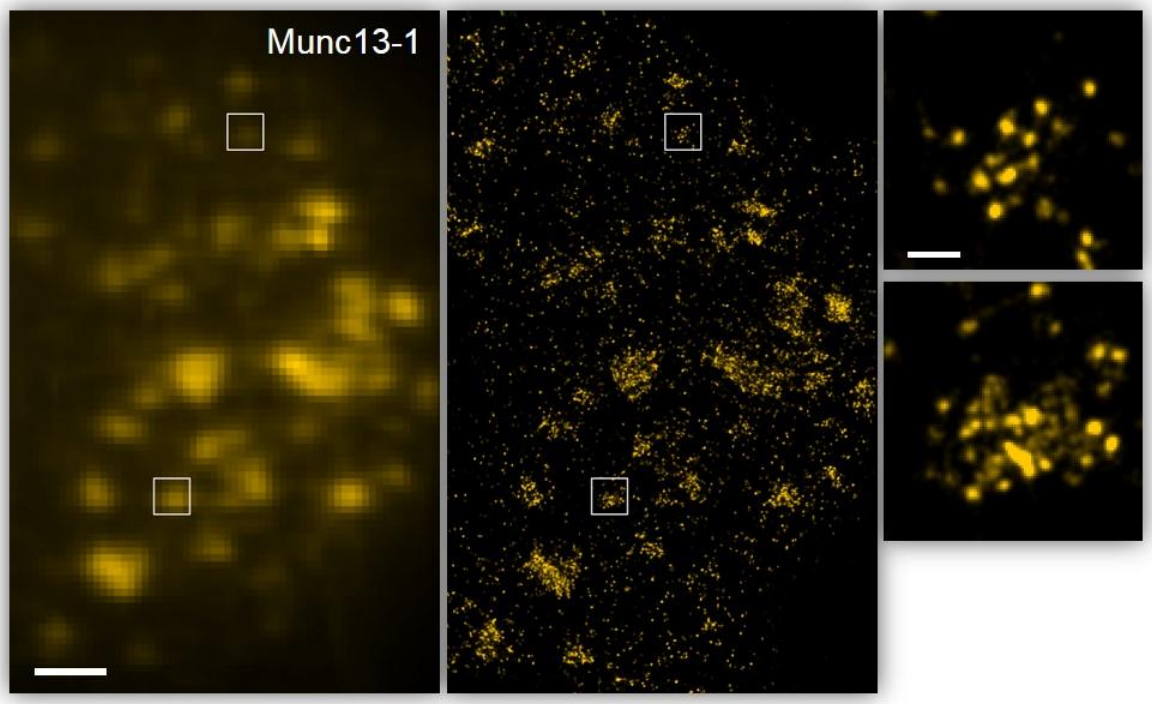

Figure 36 | STORM imaging of reconstituted Munc13-1 supramolecular assemblies in non-neuronal cells. Conventional microscopy (left) and STORM (middle) images of macromolecular self-assemblies of Munc13-1 expressed in a 293T cell. In this experiment, TagRFP-ZF-CAAX was co-expressed. Munc13-1 was immunostained with a Munc13-1 monoclonal antibody (clone: 11B-10G) and an Alexa-647 labeled secondary antibody. Right panels are enlarged views of the white-boxed regions in the middle panel. Scale bars, 2 µm and 200 nm.

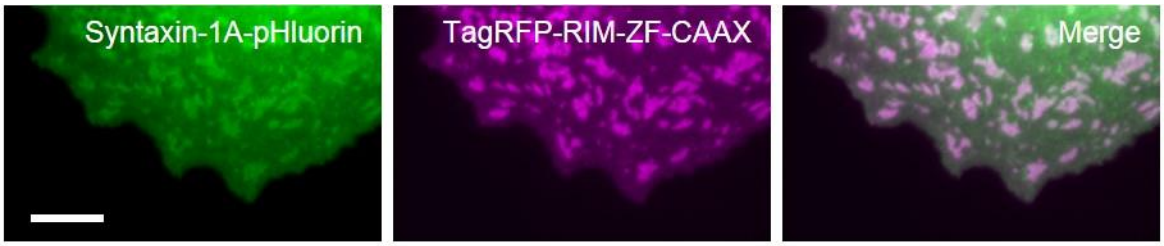

Figure 37 | Reconstitution of Munc13-1/syntaxin-1 macromolecular assemblies in non-neuronal cells. Fluorescence images of syntaxin-1A-pHluorin (left) and TagRFP-ZF-CAAX (middle) expressed in a COS7 cell. Right panel shows a merged image. Munc13-1 and Munc18-1 were also expressed in this experiment. Scale bar, 10 μm.

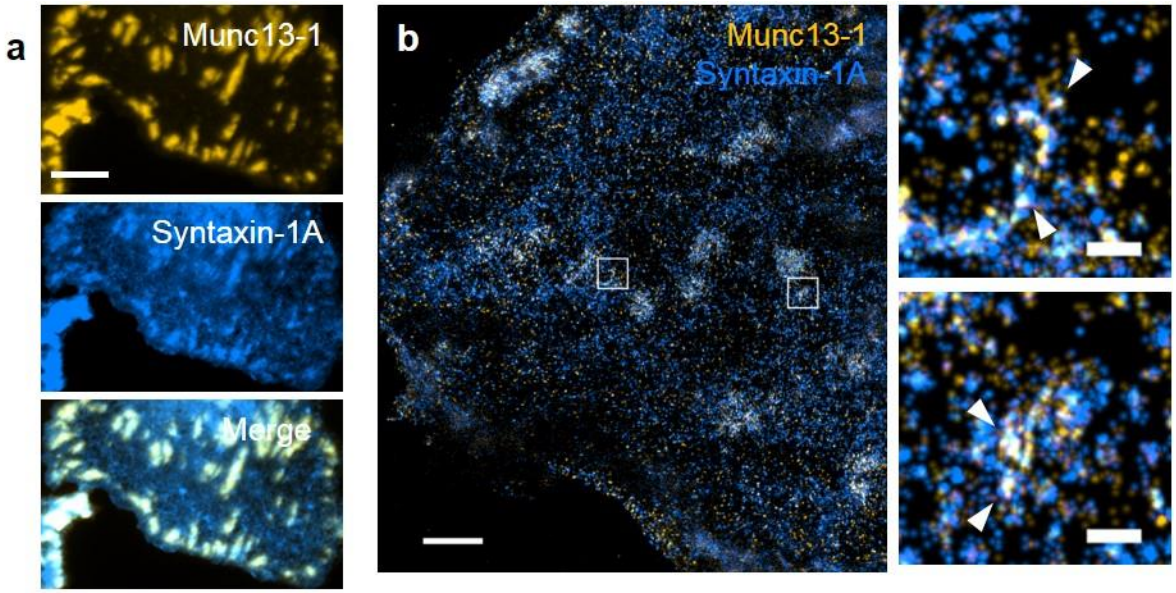

Figure 38 | STORM imaging of reconstituted Munc13-1/syntaxin-1 supramolecular assemblies in non-neuronal cells. (**a**) Immunofluorescence images of Munc13-1 (yellow) and syntaxin-1A (blue) expressed in a COS7 cell. TagRFP-ZF-CAAX and Munc18-1 were also expressed in this experiment. Scale bar, 10 μm. Selective accumulations of syntaxin-1A molecules at macromolecular self-assemblies consisting of Munc13-1 are observed. (**b**) 3D-STORM images of Munc13-1 (yellow) and syntaxin-1A (blue) expressed in COS7 cells. In this experiment, TagRFP-ZF-CAAX and Munc18-1 were also co-expressed. Right panels are enlarged views of the white-boxed regions in the left panel. Recruitments of syntaxin-1 molecules to Munc13-1 nanoscale supramolecular assemblies were reconstituted in the non-neuronal cell membrane (arrowheads). Scale bars, 2 μm and 200 nm.

Discussion

I show that Munc13-1 molecules form nanoscale supramolecular assemblies, which recruit syntaxin-1, at the cell membrane of presynaptic terminals, and hypothesize that the supramolecular assembly is the physical entity of the release site described in quantum theory [1]. It was originally suggested that Munc13-1 plays an important role in synaptic vesicle priming, a post-docking chemical process that leaves synaptic vesicles ready for release [29–32]. This process is thought to involve opening of the closed syntaxin-1/Munc18-1 complex [66, 68]. Recent sophisticated electron microscopy studies using high-pressure freezing to examine Munc13- and syntaxin-1-deficient synapses showed that these molecules are needed for docking of synaptic vesicles [69–71]; thus, docking and priming are inseparable molecular processes. I here provide advanced supramolecular mechanisms to account for docking and priming (Figure 2). At the AZ, supramolecularly assembled Munc13-1 molecules serve as a recruiting site for the syntaxin-1/Munc18-1 complex. The supramolecular assembly effectively and locally provides open syntaxin-1 molecules for use in forming active SNARE complexes and thereby specifies the site for synaptic vesicle docking, priming, and release. The supramolecular assembly constituting the quantal release site should also include proteins other than Munc13-1 such as Ca^{2+} channels. Indeed, in the Drosophila neuromuscular junction, it has been suggested that the synaptic vesicle release site most likely contains Ca^{2+} channels, Bruchpilot and Rim-binding protein other than Unc13A (the homologue of Munc13-1) [72].

Additional research is required to obtain a complete picture of the assembly.

The multiplicity of the quantal release sites implemented by discrete supramolecular assemblies of Munc13-1 within a single active zone provides a pure presynaptic mechanism for setting the synaptic strength across synapses. The average number of the quantal release sites was about 5, similar to the value for single glutamatergic synapses in the cerebellum, which was electrophysiologically determined using minimal stimulation [73], and to the value for the number of readily releasable vesicles in the cultured hippocampal neurons determined by an optical method using pHluorin [74]. Based on the present results, the number of quantal release sites varied from synapse to synapse, up to 18, which corresponds to the dynamic range of several bits as discrete strength levels. The large heterogeneity in the number of quantal release sites would provide a wide range of synaptic strength across synapses (synaptic weight) to contribute to synaptic computation.

Another important aspect of this presynaptic mechanism is that synaptic strength can be set independently of temporal dynamics at individual synapses by controlling the number of quantal release sites. Although both vesicular release probability and the number of quantal release sites can contribute to overall synaptic strength, I found that these were independently controlled and exerted different effects on the short-term plasticity of vesicular release (Figure 14 and 15), i.e., the extent of the short-term plasticity induced by repetitive action potential firing depended on the vesicular release probability, but not on the number of quantal release

sites. Therefore, the quantity of a synaptic response can be changed while retaining unique properties of temporal coding determined by vesicular release probability [75].

In my primary hippocampal cultures, the release sites were fully occupied by releasable vesicles at rest, as has been reported in some central glutamatergic synapses [23, 76]. Interestingly, the release sites appeared not always fully occupied in some glutamatergic synapses in other brain regions [73, 77]. Therefore, mechanisms other than those for the regulation of the number of release sites and the release probability might control the vesicle occupancy, which could also affect the synaptic strength and temporal codes.

Despite high variability in the number of quantal release sites among synapses, the number for each synapse was stably fixed. In my experimental setting in which no long-term synaptic plastic changes were induced, N_{RRV} was constant for at least several tens of minutes. This temporal stability should confer robustness of synaptic computation in neuronal circuits. The stability might reflect ordered spatial arrangements of Munc13-1 assemblies in the AZ, with nearly fixed size and inter-assembly distance (Figure 25) and its oscillatory distribution (Figure 26). A plausible theoretical model for explaining such ordered pattern formation is a reaction-diffusion model [78–80]. As is exemplified by a recent theoretical study of the spatiotemporal distribution of synaptic proteins [81], spatial patterns formed by molecules can be stable on a much longer time scale than that of immediate molecular interactions. In the framework of the model, molecular interactions of Munc13-1 [28, 82, 83] should play roles in

forming stable and ordered Munc13-1 assemblies. In such roles, the self-assembling property of Munc13-1 molecules may play a central role as an attractive cue for the pattern formation. The self-assembling property of biomolecules [84, 85] leading to ordered supramolecular nanostructures may be a general source of functional stability in various biological processes despite the presence of molecular noise.

References

1. Katz, B. *The Release of Neural Transmitter Substances* (Liverpool Univ. Press, Liverpool, 1969).

2. Atwood, H. L. & Karunanithi, S. Diversification of synaptic strength: Presynaptic elements. *Nat. Rev. Neurosci.* **3,** 497–516 (2002).

3. O'Rourke, N. A., Weiler, N. C., Micheva, K. D. & Smith, S. J. Deep molecular diversity of mammalian synapses: Why it matters and how to measure it. *Nat. Rev. Neurosci.* **13,** 365–379 (2012).

4. Buzsáki, G. & Mizuseki, K. The log-dynamic brain: How skewed distributions affect network operations. *Nat. Rev. Neurosci.* **15,** 264–278 (2014).

5. Barbour, B., Brunel, N., Hakim, V. & Nadal, J. P. What can we learn from synaptic weight distributions? *Trends Neurosci.* **30,** 622–629 (2007).

6. Abbott, L. F. & Nelson, S. B. Synaptic plasticity: taming the beast. *Nat. Neurosci.* **3,** 1178–1183 (2000).

7. Abbott, L. F. & Regehr, W. G. Synaptic computation. *Nature* **431,** 796–803 (2004).

8. Turrigiano, G. G. & Nelson, S. B. Homeostatic plasticity in the developing nervous system. *Nat. Rev. Neurosci.* **5,** 97–107 (2004).

9. Malenka, R. C. & Bear, M. F. LTP and LTD: An embarrassment of riches. *Neuron* **44,** 5–21 (2004).

10. Buonomano, D. V. & Maass, W. State-dependent computations: Spatiotemporal processing in cortical networks. *Nat. Rev. Neurosci.* **10,** 113–125 (2009).

11. Heuser, J. E. *et al.* Synaptic vesicle exocytosis captured by quick freezing and correlated with quantal transmitter release. *J. Cell Biol.* **81,** 275–300 (1979).

12. Rizzoli, S. O. & Betz, W. J. Synaptic vesicle pools. *Nat. Rev. Neurosci.* **6,** 57–69 (2005).

13. Peters, A., Palay, S. L. & Webster, H. D. *The fine structure of the nervous system* (Oxford University Press, New York, 1991).

14. Korn, H., Triller, A., Mallet, A. & Faber, D. S. Fluctuating responses at a central synapse: n of binomial fit predicts number of stained presynaptic boutons. *Science* **213,** 898–901 (1981).

15. Gulyás, A. I. *et al.* Hippocampal pyramidal cells excite inhibitory neurons through a single release site. *Nature* **366,** 683–687 (1993).

16. Silver, R. A., Lübke, J., Sakmann, B. & Feldmeyer, D. High-probability uniquantal transmission at excitatory synapses in barrel cortex. *Science* **302,** 1981–1984 (2003).

17. Biro, A. A., Holderith, N. B. & Nusser, Z. Quantal size is independent of the release probability at hippocampal excitatory synapses. *J. Neurosci.* **25,** 223–232 (2005).

18. Wadiche, J. I. & Jahr, C. E. Multivesicular release at climbing fiber-Purkinje cell synapses. *Neuron* **32,** 301–313 (2001).

19. Oertner, T. G., Sabatini, B. L., Nimchinsky, E. A. & Svoboda, K. Facilitation at single

synapses probed with optical quantal analysis. *Nat. Neurosci.* **5,** 657–664 (2002).

20. Christie, J. M. & Jahr, C. E. Multivesicular release at Schaffer collateral–CA1 hippocampal synapses. *J. Neurosci.* **26,** 210–216 (2006).

21. Biro, A. A., Holderith, N. B. & Nusser, Z. Release probability-dependent scaling of the postsynaptic responses at single hippocampal GABAergic synapses. *J. Neurosci.* **26,** 12487–12496 (2006).

22. Loebel, A., Silberberg, G., Helbig, D., Markram, H., Tsodyks, M. & Richardson, M. Multiquantal release underlies the distribution of synaptic efficacies in the neocortex. *Front. Comput. Neurosci.* **3,** 1–13 (2009).

23. Huang, C. H., Bao, J. & Sakaba, T. Multivesicular release differentiates the reliability of synaptic transmission between the visual cortex and the somatosensory cortex. *J. Neurosci.* **30,** 11994–12004 (2010).

24. Stevens, C. F. Neurotransmitter release at central synapses. *Neuron* **40,** 381–388 (2003).

25. Neher, E. What is rate-limiting during sustained synaptic activity: Vesicle supply or the availability of release sites. *Front. Synaptic Neurosci.* **2,** 1–6 (2010).

26. Boyken, J. *et al.* Molecular profiling of synaptic vesicle docking sites reveals novel proteins but few differences between glutamatergic and GABAergic synapses. *Neuron* **78,** 285–297 (2013).

27. Weingarten, J. *et al.* The proteome of the presynaptic active zone from mouse brain. *Mol.*

Cell. Neurosci. **59,** 106–118 (2014).

28. Südhof, T. C. The presynaptic active zone. *Neuron* **75,** 11–25 (2012).

29. Augustin, I., Rosenmund, C., Südhof, T. C. & Brose, N. Munc13-1 is essential for fusion competence of glutamatergic synaptic vesicles. *Nature* **400,** 457–461 (1999).

30. Richmond, J. E., Davis, W. S. & Jorgensen, E. M. UNC-13 is required for synaptic vesicle fusion in C. elegans. *Nat. Neurosci.* **2,** 959–964 (1999).

31. Aravamudan, B., Fergestad, T., Davis, W. S., Rodesch, C. K. & Broadie, K. Drosophila UNC-13 is essential for synaptic transmission. *Nat. Neurosci.* **2,** 965–971 (1999).

32. Varoqueaux, F. *et al.* Total arrest of spontaneous and evoked synaptic transmission but normal synaptogenesis in the absence of Munc13-mediated vesicle priming. *Proc. Natl. Acad. Sci.* **99,** 9037–9042 (2002).

33. Betz, A. *et al.* Munc13-1 is a presynaptic phorbol ester receptor that enhances neurotransmitter release. *Neuron* **21,** 123–136 (1998).

34. Weimer, R. M. *et al.* UNC-13 and UNC-10/rim localize synaptic vesicles to specific membrane domains. *J. Neurosci.* **26,** 8040–8047 (2006).

35. Limbach, C. *et al.* Molecular in situ topology of Aczonin/Piccolo and associated proteins at the mammalian neurotransmitter release site. *Proc. Natl. Acad. Sci.* **108,** E392–E401 (2011).

36. Hell, S. W. Far-field optical nanoscopy. *Science.* **316,** 1153–1158 (2007).

37. Huang, B., Babcock, H. & Zhuang, X. Breaking the diffraction barrier: Super-resolution imaging of cells. *Cell* **143,** 1047–1058 (2010).

38. Rust, M. J., Bates, M. & Zhuang, X. Sub-diffraction-limit imaging by stochastic optical reconstruction microscopy (STORM). *Nat. Methods* **3,** 793–795 (2006).

39. Heilemann, M. *et al.* Subdiffraction-resolution fluorescence imaging with conventional fluorescent probes. *Angew. Chemie - Int. Ed.* **47,** 6172–6176 (2008).

40. Van De Linde, S. *et al.* Direct stochastic optical reconstruction microscopy with standard fluorescent probes. *Nat. Protoc.* **6,** 991–1009 (2011).

41. Bates, M., Huang, B., Dempsey, G. T. & Zhuang, X. Multicolor super-resolution imaging with photo-switchable fluorescent probes. *Science* **317,** 1749–1753 (2007).

42. Huang, B., Wang, W., Bates, M. & Zhuang, X. Three-dimensional super-resolution imaging by stochastic optical reconstruction microscopy. *Science* **319,** 810–813 (2008).

43. Dani, A., Huang, B., Bergan, J., Dulac, C. & Zhuang, X. Superresolution imaging of chemical synapses in the brain. *Neuron* **68,** 843–856 (2010).

44. Takikawa, K. *et al.* High-throughput development of a hybrid-type fluorescent glutamate sensor for analysis of synaptic transmission. *Angew. Chemie - Int. Ed.* **126,** 13657–13661 (2014).

45. Kaech, S. & Banker, G. Culturing hippocampal neurons. *Nat. Protoc.* **1,** 2406–2415 (2006).

46. Shirane, D. *et al.* Enzymatic production of RNAi libraries from cDNAs. *Nat. Genet.* **36,** 190–196 (2004).

47. Tsukamoto, K. *et al.* Binding of Clostridium botulinum type C and D neurotoxins to ganglioside and phospholipid: Novel insights into the receptor for clostridial neurotoxins. *J. Biol. Chem.* **280,** 35164–35171 (2005).

48. Del Castillo, J. & Katz, B. Quantal components of end-plate potential. *J Physiol* **124,** 560–573 (1954).

49. Kuno, M. Quantal components of excitatory synaptic potentials in spinal motoneurones. *J. Physiol.* **175,** 81–99 (1964).

50. Vere-Jones, D. Simple stochastic models for the release of quanta of transmitter from a nerve terminal. *Aust. J. Stat.* **8,** 53–63 (1966).

51. Silver, R. A., Momiyama, A. & Cull-Candy, S. G. Locus of frequency-dependent depression identified with multiple-probability fluctuation analysis at rat climbing fibre - Purkinje cell synapses. *J. Physiol.* **510,** 881–902 (1998).

52. Clements, J. D. & Silve, R. A. Unveiling synaptic plasticity: A new graphical and analytical approach. *Trends Neurosci.* **23,** 105–113 (2000).

53. Silver, R. A. Estimation of nonuniform quantal parameters with multiple-probability fluctuation analysis: Theory, application and limitations. *J. Neurosci. Methods* **130,** 127–141 (2003).

54. Cohen, I., Van Der Kloot, W. & Attwell, D. The timing of channel opening during miniature end-plate currents. *Brain Res.* **223,** 185–189 (1981).

55. Kloot, W. Van der. Estimating the timing of quantal releases during end-plate currents at the frog neuromuscular junction. *J. Physiol.* **402,** 595–603 (1988).

56. Burgalossi, A. *et al.* SNARE protein recycling by αSNAP and βSNAP supports synaptic vesicle priming. *Neuron* **68,** 473–487 (2010).

57. Neher, E. Merits and limitations of vesicle pool models in view of heterogeneous populations of synaptic vesicles. *Neuron* **87,** 1131–1142 (2015).

58. Baddeley, D. *et al.* 4D super-resolution microscopy with conventional fluorophores and single wavelength excitation in optically thick cells and tissues. *PLoS One* **6,** e20645 (2011).

59. Dempsey, G. T., Vaughan, J. C., Chen, K. H., Bates, M. & Zhuang, X. Evaluation of fluorophores for optimal performance in localization-based super-resolution imaging. *Nat. Methods* **8,** 1027–1040 (2011).

60. Illian, J., Penttinen, A., Stoyan, H. & Stoyan, D. *Statistical analysis and modelling of spatial point patterns* (John Wiley & Sons, 2008).

61. Sengupta, P. *et al.* Probing protein heterogeneity in the plasma membrane using PALM and pair correlation analysis. *Nat. Methods* **8,** 969–975 (2011).

62. Veatch, S. L. *et al.* Correlation functions quantify super-resolution images and estimate

apparent clustering due to over-counting. *PLoS One* **7,** e31457 (2012).

63. Rosenmund, C. & Stevens, C. F. Definition of the readily releasable pool of vesicles at hippocampal synapses. *Neuron* **16,** 1197–1207 (1996).

64. Zucker, R. S. & Regehr, W. G. Short-term synaptic plasticity. *Annu. Rev. Physiol.* **64,** 355–405 (2002).

65. Andrews-Zwilling, Y. S., Kawabe, H., Reim, K., Varoqueaux, F. & Brose, N. Binding to Rab3A-interacting molecule RIM regulates the presynaptic recruitment of Munc13-1 and ubMunc13-2. *J. Biol. Chem.* **281,** 19720–19731 (2006).

66. Jahn, R. & Fasshauer, D. Molecular machines governing exocytosis of synaptic vesicles. *Nature* **490,** 201–207 (2012).

67. Betz, A. *et al.* Functional interaction of the active zone proteins Munc13-1 and RIM1 in synaptic vesicle priming. *Neuron* **30,** 183–196 (2001).

68. Ma, C., Li, W., Xu, Y. & Rizo, J. Munc13 mediates the transition from the closed syntaxin-Munc18 complex to the SNARE complex. *Nat. Struct. Mol. Biol.* **18,** 542–549 (2011).

69. Hammarlund, M., Palfreyman, M. T., Watanabe, S., Olsen, S. & Jorgensen, E. M. Open syntaxin docks synaptic vesicles. *PLoS Biol.* **5,** 1695–1711 (2007).

70. Siksou, L. *et al.* A common molecular basis for membrane docking and functional priming of synaptic vesicles. *Eur. J. Neurosci.* **30,** 49–56 (2009).

71. Imig, C. *et al.* The morphological and molecular nature of synaptic vesicle priming at presynaptic active zones. *Neuron* **84,** 416–431 (2014).

72. Böhme, M. A. *et al.* Active zone scaffolds differentially accumulate Unc13 isoforms to tune Ca2+channel-vesicle coupling. *Nat. Neurosci.* **19,** 1311–1320 (2016).

73. Miki, T. *et al.* Actin-and myosin-dependent vesicle loading of presynaptic docking sites prior to exocytosis. *Neuron* **91,** 808–823 (2016).

74. Ariel, P., Hoppa, M. B. & Ryan, T. A. Intrinsic variability in Pv, RRP size, Ca^{2+} channel repertoire, and presynaptic potentiation in individual synaptic boutons. *Front. Synaptic Neurosci.* **4,** 9 (2013).

75. Tsodyks, M. V. & Markram, H. The neural code between neocortical pyramidal neurons depends on neurotransmitter release probability. *Proc. Natl. Acad. Sci.* **94,** 719–723 (1997).

76. Saviane, C. & Silver, R. A. Fast vesicle reloading and a large pool sustain high bandwidth transmission at a central synapse. *Nature* **439,** 983–987 (2006).

77. Jackman, S. L. *et al.* Role of the synaptic ribbon in transmitting the cone light response. *Nat. Neurosci.* **12,** 303–310 (2009).

78. Turing, A. M. The chemical basis of morphogenesis. *Phil. Trans. R. Soc. Lond. B* **237,** 37–72 (1952).

79. Gierer, A. & Meinhardt, H. A theory of biological pattern formation. *Kybernetik* **12,** 30–

39 (1972).

80. Dehmelt, L. & Bastiaens, P. I. H. Spatial organization of intracellular communication: Insights from imaging. *Nat. Rev. Mol. Cell Biol.* **11,** 440–452 (2010).

81. Haselwandter, C. A., Calamai, M., Kardar, M., Triller, A. & Azeredo Da Silveira, R. Formation and stability of synaptic receptor domains. *Phys. Rev. Lett.* **106,** 238104 (2011).

82. Ohtsuka, T. *et al.* CAST: A novel protein of the cytomatrix at the active zone of synapses that forms a ternary complex with RIM1 and Munc13-1. *J. Cell Biol.* **158,** 577–590 (2002).

83. Wang, X. *et al.* A protein interaction node at the neurotransmitter release site: domains of Aczonin/Piccolo, Bassoon, CAST, and rim converge on the N-terminal domain of Munc13-1. *J. Neurosci.* **29,** 12584–12596 (2009).

84. Whitesides, G. M. & Grzybowski, B. Self-assembly at all scales. *Science* **295,** 2418–2421 (2002).

85. Karsenti, E. Self-organization in cell biology: a brief history. *Nat. Rev. Mol. Cell Biol.* **9,** 255–262 (2008).

Acknowledgment

I am sincerely grateful to Professor Kenzo Hirose for continuous support and valuable discussion, and Dr. Shigeyuki Namiki for continuous support. I thank Dr. Tetsuroh Ariyoshi and Dr. Naoya Kimpara for stimulating discussion and technical support. I also thank Dr. S. Kozaki (Osaka Prefecture University) for providing the BoNT/C-H_C construct, Dr. T. Kohda (Osaka Prefecture University) for preliminary preparation of the BoNT/C-H_C protein, and Dr. N. Brose (Max Planck Institute) for providing the Munc13-1-EGFP construct. I am also grateful to Dr. Kohtaroh Sugao, Daisuke Shirane, Sho Iinuma, Dr. Daisuke Asanuma, Dr. Daisuke Takei, Dr. Yusaku Ohta, Dr. Isamu Taiko, Dr. Kenji Takikawa, Dr. Masayuki Isa, Dr. Taichi Onishi, Reo Yoshioka, Rieko Tanaka, Yumiko Osakaya, and Miho Nishimura for continuous support and encouragement.